Title
Exploiting Phase Boundaries for Near-Unity CsPbBr3 Nanocrystals and Elucidating Coupling in 2D Assemblies

Author
Curling, Ethan

Publication Date
2023

Peer reviewed|Thesis/dissertation

Exploiting Phase Boundaries for Near-Unity CsPbBr3 Nanocrystals and Elucidating Coupling in 2D Assemblies

By

Ethan Bryce Curling

A dissertation submitted in partial satisfaction of the

requirements for the degree of

Doctor of Philosophy

in

Chemistry

in the

Graduate Division

of the

University of California, Berkeley

Committee in Charge

Professor A. Paul Alivisatos, Co-Chair

Dr. Archana Raja, Co-Chair

Professor Kwabena Bediako

Professor Zakaria Al Balushi

Spring 2023

Abstract

Exploiting Phase Boundaries for Near-Unity CsPbBr3 Nanocrystals and Elucidating Coupling in 2D Assemblies

By

Ethan Bryce Curling

Doctor of Philosophy in Chemistry

University of California, Berkeley

Professor A. Paul Alivisatos, Co-Chair

Dr. Archana Raja, Co-Chair

This dissertation will introduce a new synthetic method toward near-unity photoluminescence quantum yield $CsPbBr_3$ nanocrystals. The synthesis of high quality $CsPbBr_3$ was achieved through the exploitation of the delicate phase boundaries between the lead bromide phase stabilities. By stochiometrically exploring the complex and rich phase map associated with the lead bromide perovskites, deep suppression of non-radiative recombination of excitons generated upon photexcitation was achieved. In doing so, a critical ratio between bromide and lead in solution is established to reduce non-radiative recombination while maintaining phase purity. This dissertation provides additional evidence that halide vacancies are the primary contributor to non-radiative recombination in sub-stoichiometric synthesis of $CsPbBr_3$ nanocrystals. Furthermore, it is proposed that lead vacancies are responsible for non-radiative recombination in when exceeding stoichiometric ratios. The various phase stabilities responsible for the lead deficient $CsPbBr_3$ phase were identified via UV-VIS signatures. In the process, a new lead bromide magic-sized cluster was identified. Transformations of this magic-sized cluster were investigated. A ligand-mediated transformation from magic-sized cluster to an intermediate species was identified. Consequently, further comprehension of the formation of larger lead bromide perovskites was achieved.

Exciton diffusion measurements of 2D arrays of the optically efficient $CsPbBr_3$ suggest high inter-nanocrystal coupling. This was achieved through the investigation of the diffusivity of the charge transfer process as a function of temperature. Non-Arrhenius like behavior proves signatures of exciton delocalization over multiple quantum dots.

Acknowledgments

This dissertation is a dedication to the ones who have supported my along such an incredible journey. My parents, my brothers, my partner, and my friends. Thank you all for so much. I could not have done it without you all.

I have had incredible mentors throughout my undergraduate and graduate education. Dr. Mark Kearley, Dr. Yan Yan Hu, Dr. Geoffery Strouse, Dr. David Nenon, Dr. Jakob Dahl, and Dr. Paul Alivisatos were all instrumental in my journey to developing and becoming a better scientist. Thank you.

Table of Contents

List of Figures

Chapter 1: Introduction

1.1 Motivation

Semiconductors have shaped the modern world into a technology-focused society. Tracing back to the late 19th century, scientists began utilizing bulk semiconductor materials such as silicon and germanium for their unique electrical conductivity that was intermediate between conductors and insulators. The invention of the first practical semiconductor device, the transistor, in 1947 was a distinct turning point in the field of electronics. From bipolar junction transistors to complementary metal-oxide semiconductor (CMOS) transistors, the drive for faster and more efficient transistors has propelled the electronics industry forward[1].

Since then, the size of semiconductors has been trending toward a couple of 100 atoms or a few nanometers. As the size of semiconductors reaches the nanoscale, new physical and technological challenges arise, such as crystallite uniformity and surface effects, that must be addressed to continue to improve their performance and functionality[2]. This gave rise to the field of nanoscience. Semiconductor nanocrystals were found to have unique electronic and optical properties that can be exploited for a variety of applications such as photovoltaics and light-emitting diodes.

As semiconductors get smaller, delicate control over size and composition becomes important for more efficient photophysical or energy transfer properties. Precision at the nanoscale is challenging due to the large surface area to volume ratio which significantly increases the number of atoms on the surface[3]. Surface atoms at the nanoscale have a higher energy when compared to their bulk counterparts due to reduced coordination; therefore, a pristine surface is often hard to achieve due to defects that reduce the total energy of the nanocrystal[4]. This dissertation will explore the leveraging of material design principles to synthesize near-perfect semiconductor nanocrystals and investigate the energy transfer mechanisms present.

1.2 Semiconductor Nanocrystals and Band Structure

Although semiconductor nanocrystals, commonly referred to as quantum dots, pose challenges due to their small size, they offer several benefits that surpass those of bulk materials. One such advantage is the ability to tune their electronic properties, which enhances the optical and electronic performance of devices that utilize these materials[5,6,7]. This capability is rooted in the specific position of the electronic band structure in semiconductors.

Electronic band structures are a continuum of states that electrons can occupy. Individual electrons occupy atomic orbitals in individual atoms. When we combine multiple atoms to make molecules, these atomic orbitals hybridize to create bonding molecular orbitals that are lower in energy than their constituent atomic orbitals and stabilize the bond between the atoms. The same principles apply in extended solids, where thousands of atoms may be present. The many atomic orbitals in the solid combine are so finely spaced that they create band-like structures which dictate

the electronic and optical properties. Semiconductors, like their molecular counterparts' highest occupied molecular orbital (HOMO) and lowest occupied molecular orbital (LUMO), have occupied and unoccupied bands, namely the valence band and the conduction band respectively (Figure 1.1a). The space between, known as the band gap, and the distribution of electrons within these bands is dependent on the composition of the solid and the electron interactions within. There are two types of band gaps: direct and indirect. This describes the arrangement of the conduction band minimum (CBM) and the valence band maximum (VBM) in the momentum space. In a periodic crystal lattice, the electronic states of the material can be described by Bloch wavefunctions, which are a product of a plane wave and a periodic function with the periodicity of the crystal lattice[8]. The wavefunctions described are often characterized by their wave vector, k. The band extrema, the VBM and CBM, in the k-space can occur at different k points resulting in an indirect band gap[9]. The excitation of an electron from the valence band into the conduction band leaves behind a positively charged displacement of electrons known as a hole. For an electron to undergo excitation an indirect band gap system, momentum conservation requires a phonon, a lattice vibration, whereas in a direct band gap system, no phonon is necessary. The coulomb interaction between the positive hole in the valence band and the negative electron in the conduction band leads to a bound pair known as an exciton.

As semiconductors approach the nanoscale, the exciton begins to experience confinement of their wavefunction from the physical boundaries of the crystallite. The degree to which the exciton is confined dictates the state composition near the band edge. As the degree of confinement decreases, band edge states converge to discrete states and when confined in all dimensions, degenerate states at the same energy arise. Quantum dots experience confinement in all 3 dimensions therefore 0-dimensional confinement will be the main focus of this dissertation. Quantum dots experiencing confinement in all dimensions cause discernable changes to the band gap when the size of the crystal changes (Figure 1.1b). The band gap energy is inversely related to the size of the nanocrystal. This leads to the ability to tune the optical and electronic properties, a phenomenon known as band gap engineering. Since the properties of the nanocrystals change with size, uniformity amongst them is critical to achieving consistent and predictable material behavior and performance in various applications[10–13].

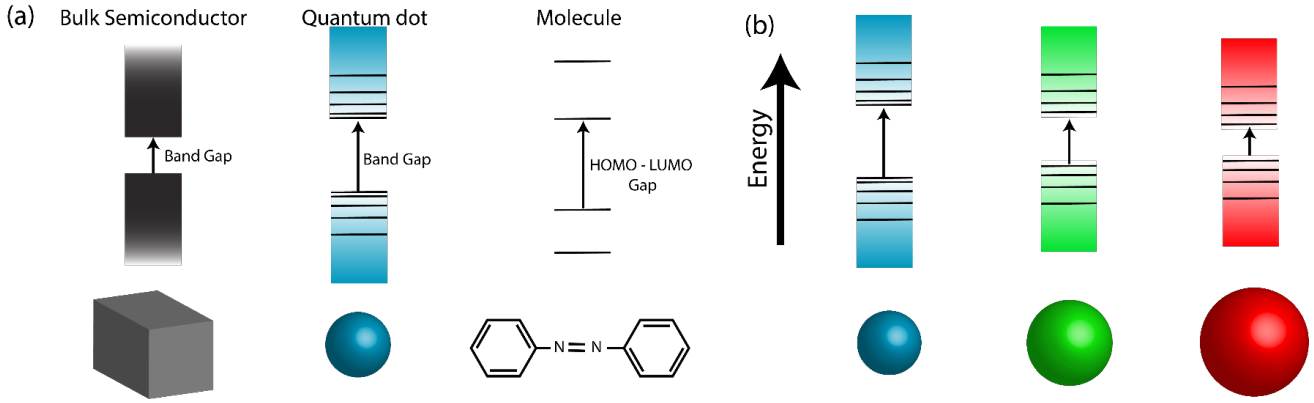

Figure 1.1: (a) A schematic representation of the differing electronic structures for bulk semiconductors, quantum dots, and molecular species. (b) A schematic representation of the size-dependent band gap of quantum dots.

Achieving high uniformity in semiconductor nanocrystals is challenging due to complex growth processes. Since the early 1950s, the investigation into the formation of colloidal crystallites garnered much attention from the materials science community. Discussion of such was pioneered by LaMer, where he proposed that temporally discrete regimes of crystallite burst nucleation and diffusion-limited growth successfully modeled the formation of crystallites in a solution[14]. Following these principles nearly 50 years later, reports of monodisperse colloidal nanocrystals began appearing in the scientific literature[15]. Informed by LaMer's model, supersaturation of the solution with a precursor through a hot-injection method proved beneficial to the formation of monodisperse nuclei. Kinetic and thermodynamic screening of precursors allowed for homogenous growth conditions, which were often informed by the synthesis of bulk materials[16]. Iteration and experimentation over the next 10-15 years resulted in the development of advanced synthesis techniques that further improved the size uniformity of semiconductor nanocrystals[17–21].

In conjunction with a strongly bound exciton, discrete band-edge states and uniform size distribution point toward a narrow linewidth and strongly luminescent nanocrystal; however, initial semiconductor nanocrystals were weakly luminescent[22–24]. Outlined in further detail in the next section, the competition between radiative and nonradiative recombination of excitons significantly affects the luminescence of the nanocrystals, and ultimately determines the efficiency of light emission from the material.

1.3 Quantum Dot Photophysics

Due to the continuum of states higher in energy than the band edge, quantum dots have broadband absorption, meaning they can absorb photons higher in energy than their band gap (Figure 1.2a). Excess energy is shed through lattice vibrations of the crystal structure, phonons, that rapidly relax the electron and hole to the band edge where they recombine. The way in which recombination of the exciton occurs is critical. The electron and hole can either recombine radiatively, emitting a photon equal to the energy of the band gap, or nonradiatively, releasing energy as thermal phonons. The relationship between these is known as the photoluminescent quantum yield (PLQY). The PLQY of a system is strongly dependent on the kinetics of both the radiative and nonradiative rates (Equation 1.1):

$$PLQY = \frac{k_r}{k_r + k_{nr}} \tag{1.1}$$

The radiative rate of a system is dependent on the properties of the electronic states responsible for the transition and the local density of electromagnetic states that the photon can emit into. The radiative rate is intrinsic to a material in a homogenous medium, therefore, is fixed. The competing pathway, nonradiative recombination, is the limiting factor in achieving high PLQY in a semiconductor nanocrystal.

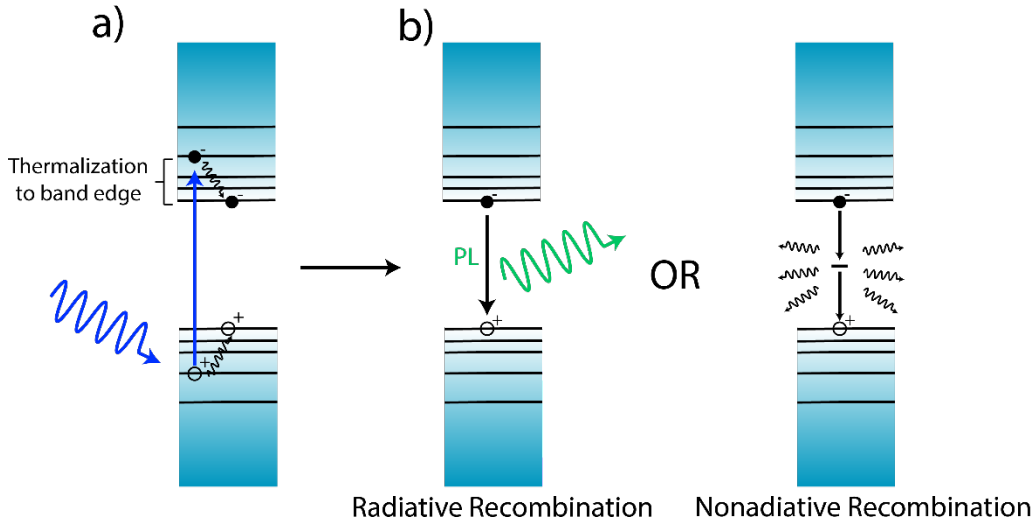

Figure 1.2: (a) A schematic representation of the excitation and thermalization of electrons and holes to the band edge. (b) A representation of the two deexcitation pathways for excitons.

The nonradiative pathways of a system are dictated by defects in the crystal structure or poor passivation at the surface. Defects and poor passivation, explored more deeply in the following section, lead to electronic states existing within the band gap which can act as recombination centers for the excited carriers (Figure 1.2b). This leads to phonon-assisted nonradiative recombination and decreased photoluminescence efficiency. Phonon-assisted recombination can still occur in perfect nanocrystals but is largely dependent on the energy of the band gap. Defect-free high band gap materials are often less susceptible to nonradiative recombination due to excitons needing to couple to multiple phonon modes to dissipate a large amount of energy[25]. For this dissertation, phonon-assisted recombination across the band gap is likely due to defects as the band gap is in the visible. As such, PLQY can be an effective probe into the quality of the nanocrystal ensemble being measured. In this dissertation, the suppression of surface defects of the $CsPbBr_3$ perovskite nanocrystals will be explored to maximize the PLQY.

1.4 Quantum Dot Surface Chemistry and Defects

Bulk semiconductors are known to contain a range of defects, including lattice dislocations, vacancies, and atoms in interstitial positions, among others. Defects interrupt the periodicity of the atomic structure of a crystal and deposit local electronic states within the band gap, greatly reducing the optoelectronic performance of the devices integrated with these materials. Bulk defects are thermodynamically unavoidable in a crystal above 0 K. According to thermodynamics the free energy of a closed system is given by:

$$\Delta G = \Delta H - T\Delta S \tag{1.2}$$

The formation of isolated point defects in a crystalline solid raises the internal energy of the system and the enthalpy of the defect formation process is endothermic. Although enthalpic formation energy is unfavorable, the configurational entropy of the system more than compensates for it[26]. This proves that bulk defects are always present in any crystalline solid above 0 K. Despite this, the defect concentration per volume in bulk semiconductors at thermodynamic equilibrium is typically low, having been reduced through the improvement of synthesis methods[27–29]. Since defect density is independent of size, defect densities would be assumed to be extremely low in small-volume crystallites such as quantum dots; however, as previously stated, the surface area to volume ratio increases greatly as the crystal reaches the nanoscale. Surface atoms are left with undercoordinated molecular orbitals, introducing energy levels within the band gap and promoting nonradiative recombination. Surface defects are the most prevalent type of defect in semiconductor nanocrystals and eliminating them has been a major focus of synthetic optimization efforts[30–32].

Colloidal semiconductor nanocrystals are comprised of a solid crystalline core surrounded by a shell of organic capping molecules (Figure 1.3a), known as ligands, that serve two purposes: to passivate the dangling bonds on the surface and to suspend nanocrystals in a solvent. Typical ligands are comprised of a long alkyl chain that provides colloidal stability and a head group that binds to the surface. The adsorption of ligands to the surface of a nanocrystal is compared to the formation of self-assembled monolayers on a flat surface[33]. The bulky steric properties of long alkyl chains play a significant role in how these ligands assemble on the surface of the nanocrystal and can sometimes impede efficient adsorption[34]. Both the binding affinity of the head group to the surface and the self-assembly of the long alkyl chains determine the equilibrium of bound versus unbound ligands in the colloidal system[35]. Head group binding of the undercoordinated surface atoms eliminates in-gap states thus suppressing nonradiative recombination of photogenerated excitons and increasing the PLQY of the system.

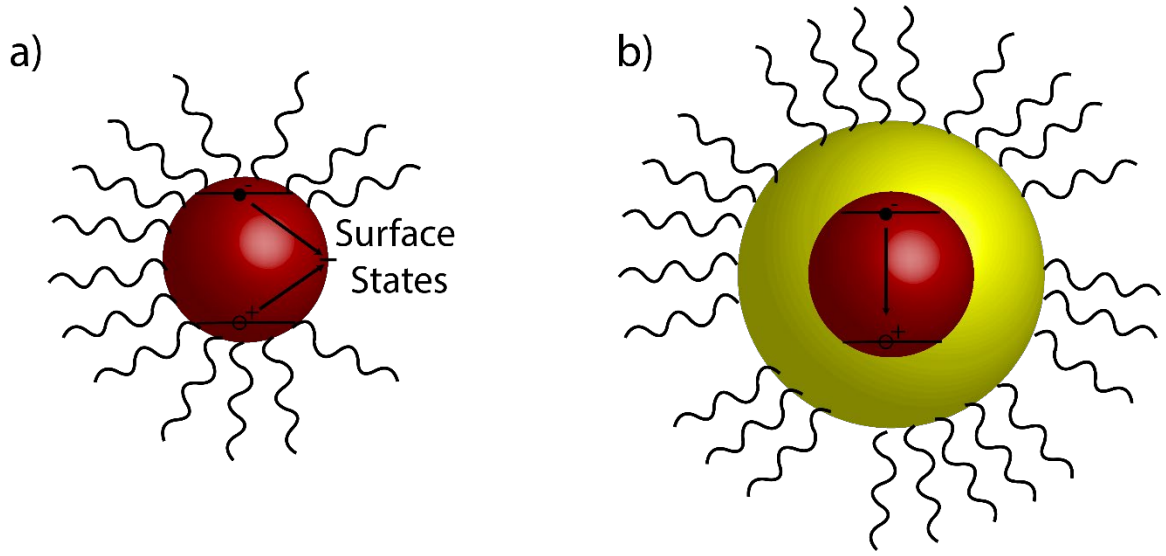

Figure 1.3: A schematic representation of a core (a) and a core/shell (b) nanocrystal. The wavy black lines represent the ligands bound to the surface while the solid black lines represent electronic states within the nanocrystal.

To overcome the complexity of ligand adsorption to attain optically efficient systems, inorganic shelling of a greater band gap material was achieved[36]. The inorganic shell was used to energetically separate charges from undesirable surface traps (Figure 1.3), therefore greatly enhancing the PLQY of the system. Localizing charges away from the surface, while beneficial for radiative recombination, can be deleterious for charge extraction from the system. The diffusion of charges within a nanocrystal solid is essential to many applications, such as photovoltaics[37]. Exploration of high-efficiency unshelled systems is essential to broader applications where charge extraction is vital to performance. The all-inorganic perovskites, specifically $CsPbBr_3$, have been proven to be optically efficient without a shell. This is a result of a defect-tolerant band structure, explored extensively in Chapter 2, resulting from the ionic nature of lead-halide octahedra responsible for the optical transition. Even with high defect tolerance, the $CsPbBr_3$ nanocrystals are still plagued by surface traps which inhibit near unity quantum yields. This thesis will focus on the suppression of these surface defects to approach the thermodynamic limit of quantum efficiencies. Exploration of how charges diffuse in an optimized, high PLQY system is essential to the design and development of efficient optoelectronic devices.

1.5 Exciton Diffusion and Quantum Dot Coupling

Nanoscale energy transfer is omnipresent in all photosystems. From plants to photovoltaic cells, understanding the energy transfer mechanism can be insightful into the architecture of high-performance materials. In plants, incident light is absorbed by a densely packed array of chlorophylls which quickly transfer the energy to reaction centers where it can be converted into useful products. Similarly, in photovoltaic cells, high energy charges are generated by the absorption of sunlight and must be transported to electrodes efficiently. Enhanced absorption of semiconductor nanocrystals has led researchers to put significant effort into designing devices utilizing their unique properties[38]. Like chlorophyll, each quantum dot acts as an absorption center for incident light and must efficiently transfer charges in a densely packed array of dots. Typically, excitons are localized to a single quantum dot and undergo a series of hops whereby the exciton hops from dot to dot as it diffuses through the accessible energy landscape.

Exciton diffusion in a quantum dot solid is enabled by Förster resonant energy transfer (FRET). In contrast to colloidally stable quantum dots, close-packed films enable coupling between dots. The Förster equation contextualizes the necessary optoelectronic and structural requirements to promote energy transfer between coupled quantum dots[39]:

$$\frac{1}{\tau_{DA}} = \frac{2\pi}{\hbar}\frac{\mu_D^2\mu_A^2\kappa^2}{r_{DA}^6 n^4} \tag{1.3}$$

The hopping rate between the quantum dots ($\frac{1}{\tau_{DA}}$), where τ_{DA} is the average time for an exciton to hop between a donor and an acceptor, is dependent on the spectral overlap between

donor (D) and acceptor (A) $\mu_D^2\mu_A^2$, the interparticle distance r, the dipole orientation factor κ, and the refractive index n. The bound electron-hole pair will hop through the accessible energy landscape until they radiatively or nonradiatively recombine. Optimization off all parameters is necessary to avoid the suppression of energy transfer in quantum dot solids. Two characteristic parameters, the diffusion length (L) and diffusivity ($cm^2\ s^{-1}$), are often the focus of the diffusion studies. The diffusion length is the average dispersion of an exciton from a single excitation site while the diffusivity reflets the rate at which the exciton is diffusing.

To overcome the limitations of FRET mediated exciton transport, the quantum mechanical effect of delocalization can be exploited. Exciton delocalization is the delocalization of the electron and hole pair over many quantum dots. Once delocalized, the exciton can undergo supertransfer between dots via constructive interference with individual quantum dot's dipole moments[40]. Achieving delocalization proves difficult due to the weak coupling between quantum dots. Insulating organic ligand shells on the nanocrystals provide barriers decrease coupling and separate the quantum dots in thin films. This is detrimental as the nearest neighbor dipole-dipole coupling between dots is defined by:

$$V = \frac{\kappa\mu^2}{\varepsilon R^3} \tag{1.5}$$

Where μ is the transition dipole, κ is the orientation factor, ε is the dielectric constant and R is the distance between the quantum dots. When the coupling between quantum dots reaches a certain threshold, the optical properties of individual nanocrystals become more coherent as the individual dipoles of multiple quantum dots combine to form a larger dipole. This phenomenon, commonly referred to as superradiance, and has been observed in various quantum systems[41,42]. Coherent emission from individual emitters results in faster and more efficient emission than any single emitter. Superradiance has substantial applications in the optoelectronics field, by boosting the performance of devices, and in the quantum information field, the entanglement of quantum bits[43]. Several techniques have been used to enhance the interaction between quantum dots, including the use of molecular linkers[44], fused dimers[45,46], and self-assembly methods[47]. Both super-transfer and superradiance via delocalization of excitons prove to be essential to the engineering of next-gen devices. A rich comprehension of the systems that can exhibit this behavior is critical to achieve this goal. Recently, $CsPbBr_3$ has been targeted as a candidate due to the high monodispersity and close-packing efficiency of these nanocrystals. This thesis will focus on the further exploration of enhancing the coupling between $CsPbBr_3$ quantum dots and the resulting exciton diffusion and optical properties associated.

Chapter 2: Synthesis and Characterization of Near-Unity $CsPbBr_3$ Nanocrystals

2.1 Synthetic Protocols

Chemicals*:*

Cesium Carbonate (99.9%, Aldrich), Lead(II) Acetate Trihydrate (99%, Alfa Aesar), 1-Octadecene technical grade (90%, Aldrich), Oleic Acid technical grade (90%, Aldrich), Oleylamine technical grade (70%, Aldrich), Benzoyl Bromide (99%, Spectrum)

Synthesis of $CsPbBr_3$ Nanocrystals:

$CsPbBr_3$ nanocrystals were synthesized using a previously established synthetic method[48]. For a standard reaction, 15 mL of 1-octadecene, 3 mL of oleylamine, 0.9 mL of oleic acid, 228 mg of lead(II) acetate trihydrate, and 48 mg of cesium carbonate were loaded into a 3-neck round bottom flask with a glass thermocouple adapter, a silicone septum and a glass air condenser connected to a Schlenk line. H-grease was used on all ground glass joints to ensure a proper seal at high temperatures. The flask was then degassed at 100 ℃ for 60 minutes. After degassing, the reaction flask was heated to 130 ℃ and filled with an argon environment using standard Schlenk line techniques. This is done to ensure the full dissolution of all precursors. Once the solution was clear (usually after around 60 minutes), the flask was cooled to 100 ℃ to be degassed for another 60 minutes. A second degassing is done to ensure that any excess water made during precursor dissolution is removed before injection. The solution in the 3-neck flask should remain clear as it is cooled. If the solution becomes cloudy again, likely due to the precipitation of precursors, heating the flask to 130 ℃ again is essential to the quality of the synthesis. Then the reaction was placed back under an inert argon atmosphere and heated to 170 ℃. Once the injection temperature was reached, 0.21 mL of benzoyl bromide was swiftly injected into the silicon septum. Immediately upon injection, the reaction was cooled in an ice bath. At 80 ℃, 20 mL of hexane was injected into the septa to solubilize a small fraction of nanocrystals that can later be isolated with size-selective precipitation. After fully cooling, the reaction mixture was then transferred via syringe into a centrifuge tube to begin the size-selective precipitation.

Stochiometric exploration of the Br:Pb ratio was conducted in this doctoral work. The 0.21 mL of benzoyl bromide described above was a 3:1 Br:Pb ratio. All other ratios explored were simply an increase in the benzoyl bromide added relative to the ratio increase.

Size Selective Precipitation:

The synthesis yields a cloudy, green solution. The cloudy reaction mixture is centrifuged at 5000 rpm for 5 minutes. The result should be a clear supernatant with a large green pellet at the bottom of the centrifuge tube. The supernatant is transferred to another centrifuge tube while the pellet is used for further characterization or discarded. To remove a small size fraction of nanocrystals, the solubility equilibrium must be shifted. By adding 20 mL of hexane to the solution previously, we can now leverage that to shift this equilibrium. To leverage this, a septum is then added to the centrifuge tube with the supernatant, and argon is sparged through the supernatant

until the reaction mixture turns cloudy. This process can be expedited by placing the centrifuge tube into a warm water bath to facilitate evaporation of the hexane. The sparging should be continued until ~15 mL of the hexane is evaporated from the solution. The solution should progress from a clear green solution to a cloudy solution. Once the solution is cloudy, it is centrifuged at 10000 rpm for 5 minutes. The result should be a clear green supernatant with a small green pellet at the bottom of the centrifuge tube. The supernatant is discarded while the precipitated pellet is transferred to the glovebox in the same centrifuge tube. The pellet is redispersed in 3 mL of anhydrous toluene in the glovebox for long-term storage and further characterization. A schematic of the size-selective precipitation process can be seen below.

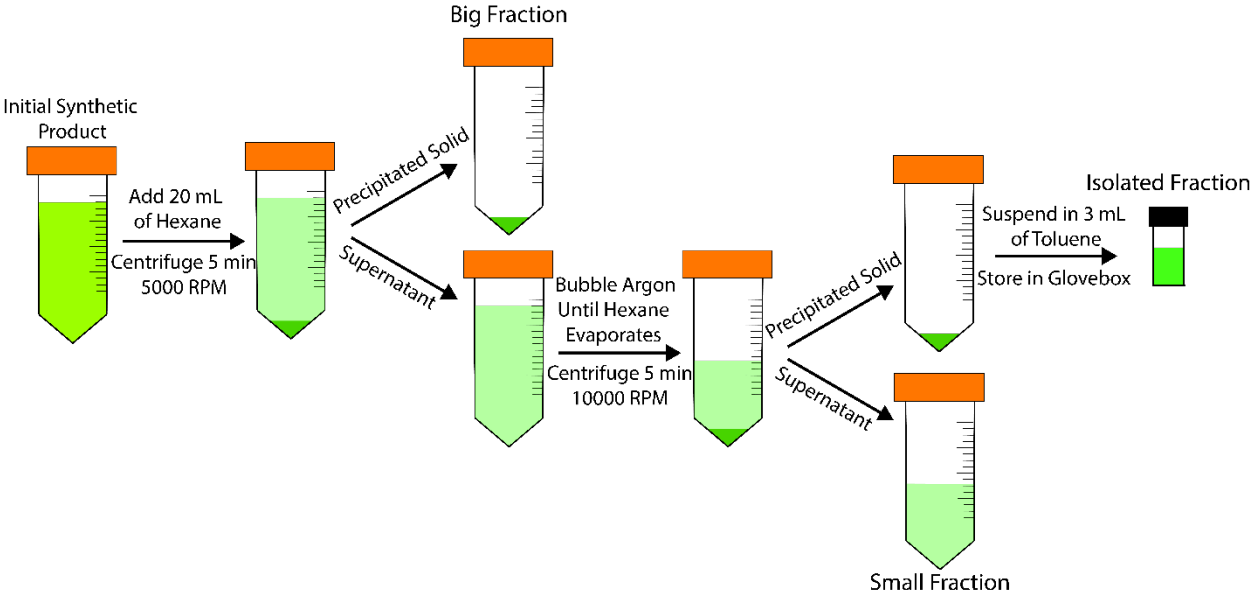

Figure 2.1: Schematic of size-selective precipitation employed to both decrease size distribution and ensure phase pure $CsPbBr_3$ cubes were collected for the isolated sample.

The goal of this doctoral work was to create synthetic conditions that suppressed non-radiative recombination in the $CsPbBr_3$ nanocrystals. A feedback loop between structural (TEM and XRD) and optical characterization (UV-VIS, PL, PLQY, PTQY) was essential to the success of this project, as it allowed for the optimization of the synthetic conditions to achieve the synthesis of high-quality $CsPbBr_3$ nanocrystals. By systematically adjusting various parameters such as the precursor concentration, reaction time, and temperature, we were able to fine-tune the properties of the nanocrystals and minimize non-radiative recombination. The feedback loop between structural and optical characterization enabled us to accurately monitor and characterize the changes in the nanocrystal structure, physical and electronic, and ultimately led to the development of a highly efficient and phase pure $CsPbBr_3$ nanocrystal synthesis. In pursuit of this, exploration of the lead perovskite phase space leads to the discovery of potential magic-sized clusters which provides further insight into the formation of lead halide perovskites.

2.2 Structural Characterization

After isolating a sample of nanocrystals, they were characterized using two standard techniques. Transmission electron microscopy allows for the confirmation of the size and shape of the nanocrystals. Powder X-ray diffraction is used for phase confirmation of the nanocrystals.

Transmission Electron Microscopy (TEM): TEM images were acquired using an FEI Tecnai T20 transmission electron microscope equipped with a Gatan RIO16IS camera and a LaB6 filament. Images were captured under a 200 kV accelerating voltage. Samples were drop-cast on a carbon support with 400 copper mesh.

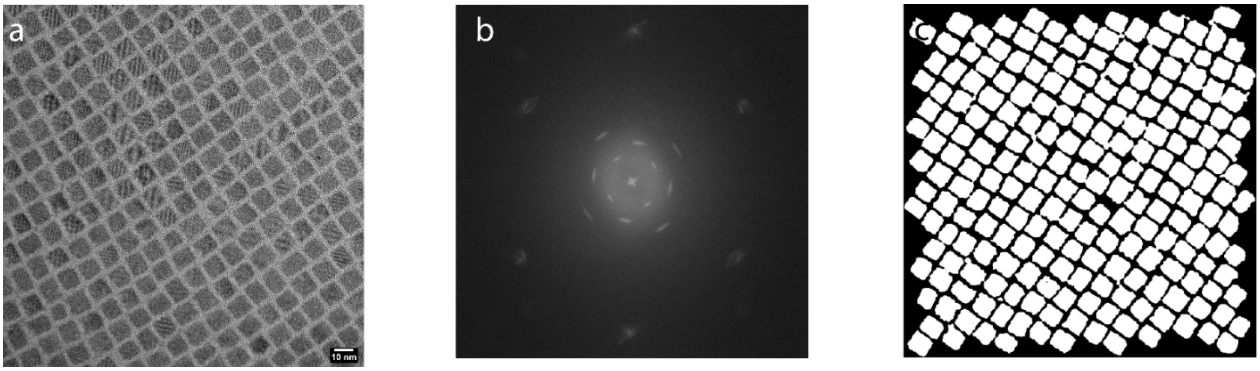

Figure 2.2: a) TEM image and b) the fast Fourier transform and c) binary image used to calculate particle area of the as-synthesized $CsPbBr_3$ nanocrystals.

Bright-field TEM (Figure 2.2A) reveals the cubic nature of the nanocrystals with an average area of 110 $\pm$ 8 nm^2. Considering the particles as cubes, we calculate an average edge length of 10.5 $\pm$ 0.4 nm and an interparticle spacing between the cubic superlattice is 2.5 nm from the resulting organic ligand shell.

Powder X-ray diffraction (XRD): XRD Patterns were collected using a Bruker D2 Phaser X-ray diffractometer equipped with a Cu Kα wavelength of 1.5445 Å. Samples were drop-cast on a silicon wafer and dried under air flow before measurement. Each measurement was collected for 45 minutes.

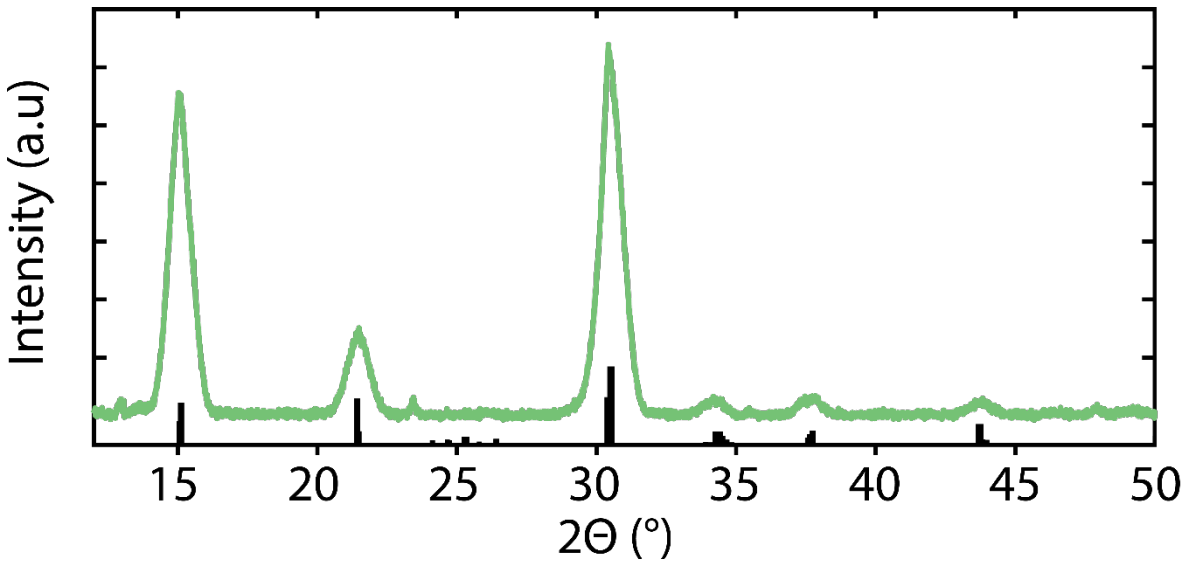

Figure 2.3: A representative X-ray diffraction pattern of $CsPbBr_3$ nanocrystals together with the simulated reference pattern for cubic $CsPbBr_3$.

2.3 Optical Spectroscopy

Optical measurements conducted on the $CsPbBr_3$ nanocrystals in this study were performed on dilute samples (100x dilution from stock) in toluene. All samples were prepared in an inert atmosphere glovebox and sealed to ensure no degradation or changes occurred.

UV/VIS: Absorption spectra were collected with a Shimadzu UV-3600 double-beam spectrometer under the slowest scanning settings and a 1 nm slit width.

Steady-State Photoluminescence: Photoluminescence (PL) measurements were conducted on a Horiba Jobin-Yvon Fluorolog steady-state spectrometer. The light source is a 437nm diode. Spectra were integrated at 0.1s/nm.

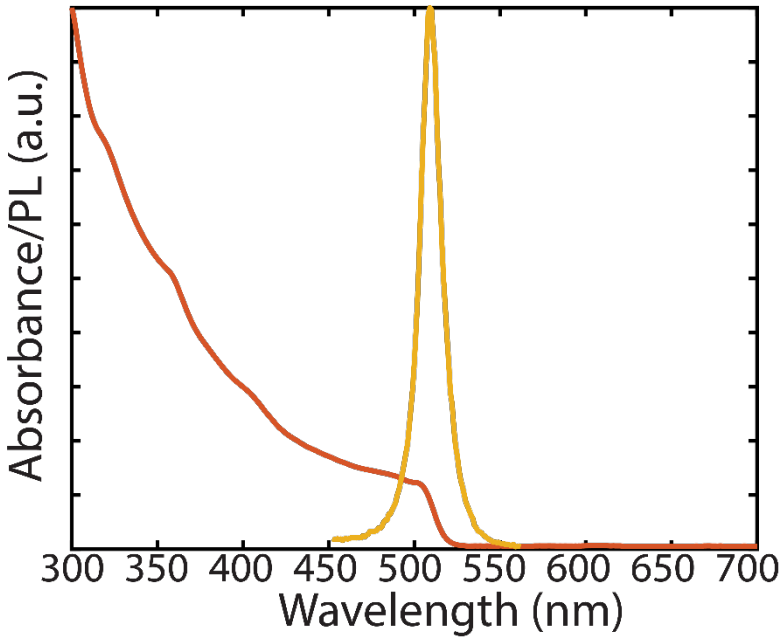

Figure 2.4: A representative absorbance and steady-state PL measurement for $CsPbBr_3$ nanocrystals with a photoluminescence center wavelength of 509 nm.

Steady-state PL can also evaluate the crystallite size and size distribution of the as-synthesized nanocrystals. The results of the size-selective precipitation are reflected by the change in full-width half max (FWHM) of the photoluminescence profile. A blue shift from the total sample to the isolated sample is expected as the isolation of smaller particles is achieved. (Figure 2.5).

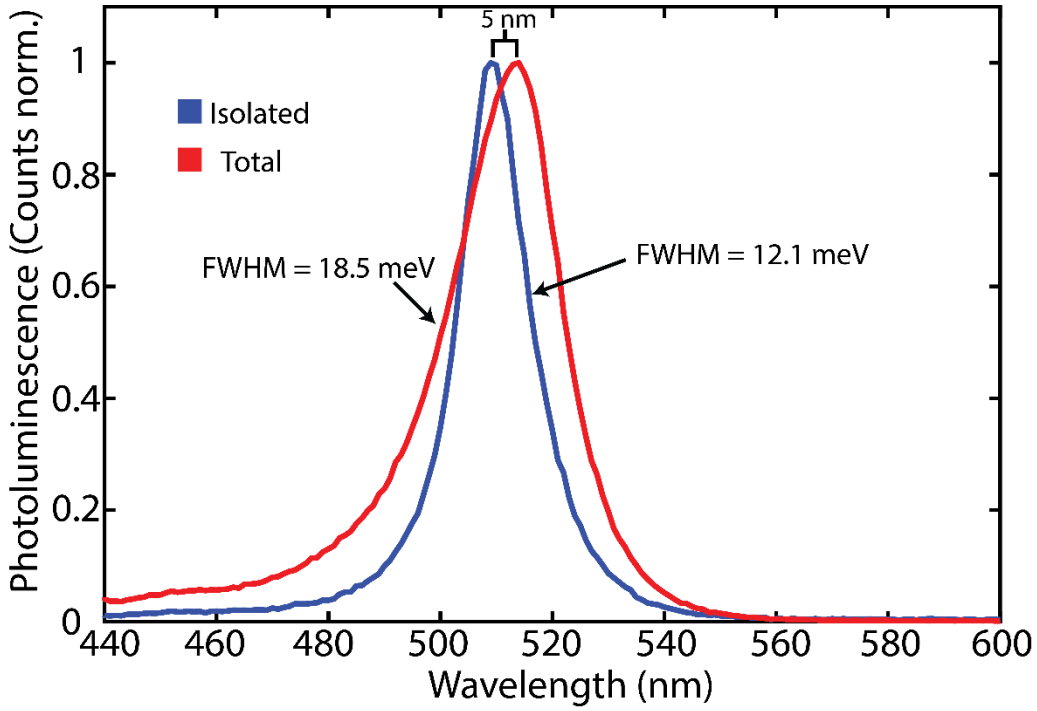

Figure 2.5: Photoluminescence spectra comparing the isolated fraction, obtained using the size-selective precipitation shown above, from the total sample. A clear decrease in FWHM is observed and a small blue shift of 5 nm is observed. The sample was excited at 420 nm. The total sample peak position is at 514 nm while the isolated sample is at 509 nm.

Time-Resolved Photoluminescence (TRPL): Photoluminescence Lifetimes were measured using a PicoQuant Fluotime 300 equipped with a PMA 175 detector and an LDH-P-C405 diode laser with an excitation wavelength of 407 nm. Although repetition rates of up to 80 MHz were possible, repetition rates were adjusted per scan to observe the whole decay.

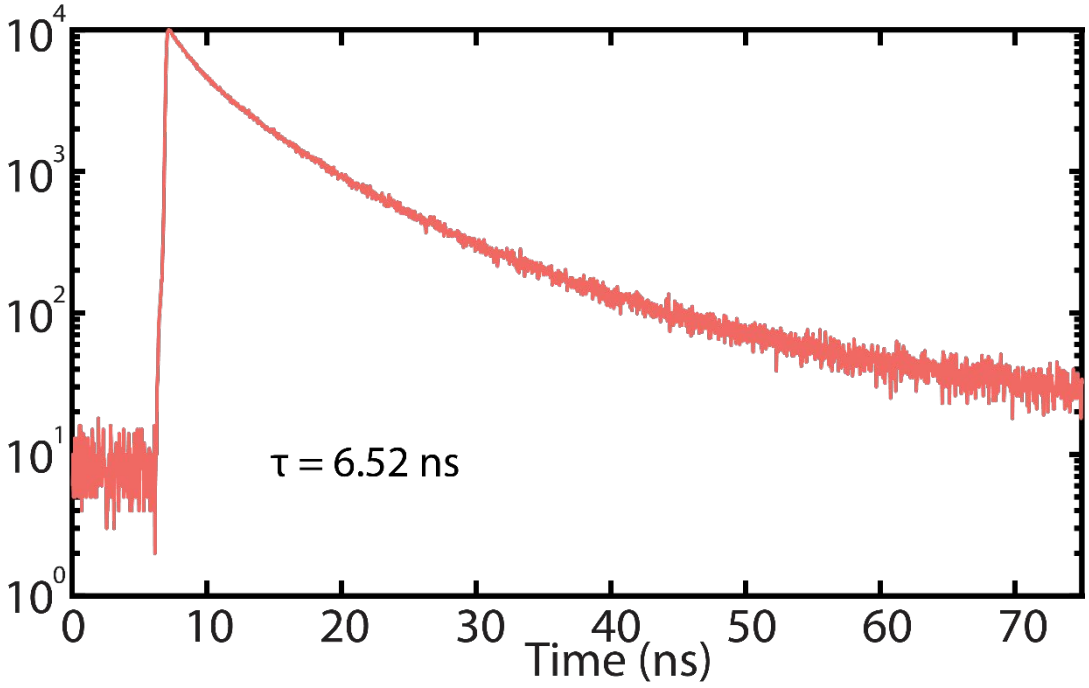

Figure 2.6: A representative time-resolved photoluminescence decay of the $CsPbBr_3$ nanocrystals.

The TRPL decay of the $CsPbBr_3$ displays multiexponential behavior which is indicative of charge trapping. The focus of this thesis work is to create synthetic conditions that suppress these undesirable trap states and increase the monoexponential character of the decay.

Photoluminescence Quantum Yield Measurements (PLQY): PLQY measurements were conducted on a home-built integrating sphere spectrofluorometer. A fianium SC450 pulsed supercontinuum laser provides white light that is then filtered with two monochromators, a Princeton SP150, and a Princeton SP275. The monochrome light is then sent through a beam splitter to a photodiode to measure power and to a Spectralon coated LabSphere integrating sphere. The sample is held opposite to the entrance port of the integrating sphere in a circular quartz cuvette. To prevent direct reflection, a baffle is fitted to the inside of the sphere. The diffuse light leaving the integrating sphere is then focused into a Princeton SP2300 monochromator. This spectrum is detected with a Princeton PIXIS 400B electrically cooled CCD at -50°C. A more detailed description of the home-built integrating sphere spectrofluorometer can be found in *Bronstein et al*[49].

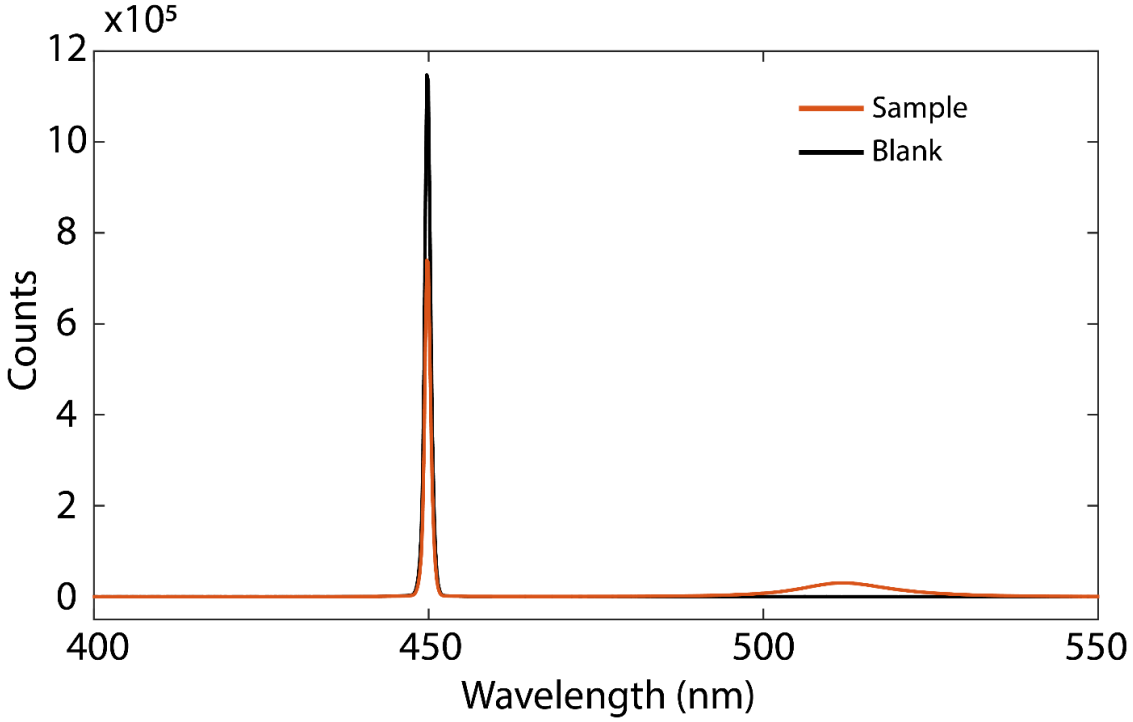

Figure 2.7: A representative spectra used to calculate the PLQY of the $CsPbBr_3$ nanocrystals. This spectrum was taken under 450 nm excitation for both the blank and the sample. The sample and the blank are scanned 5 times at varying wavelengths above the band gap using the home-built integrating sphere setup. The absorbance of the laser by the sample is shown by the change in intensity of the laser between the blank and the sample spectra. A rise in intensity at ~510 nm reflects the photoluminescence of the sample.

Photothermal Threshold Quantum Yield (PTQY): PTQY measurements were conducted on a home-built photothermal deflection spectrometer coupled with photoluminescence detection. Excitation, provided by a 150W xenon lamp, was monochromated and filtered before being chopped using a mechanical chopper. To increase the excitation area of the sample, the light was imaged as a rectangle onto the sample. A focused HeNe laser was aligned transverse to the excitation and as close to the sample as possible. Deflection of the HeNe was detected using a 1D position-sensitive diode. Photoluminescence of the sample was outcoupled via free-space to fiber and then passed to a monochromator and CCD for detection. A more detailed description of the home-built PTQY setup can be found in Hanifi *et al*[50]. Samples were prepared by drop-casting the concentrated stock $CsPbBr_3$ solution (~2 μM) in an inert environment glovebox onto a quartz substrate. For even evaporation over the sample surface, a 20 mL glass beaker was placed over the drop-casted substrate to slow the evaporation of toluene, the solvent. The substrate was then loaded into a cuvette holder containing the deflection media and sealed to ensure air-free conditions during measurement.

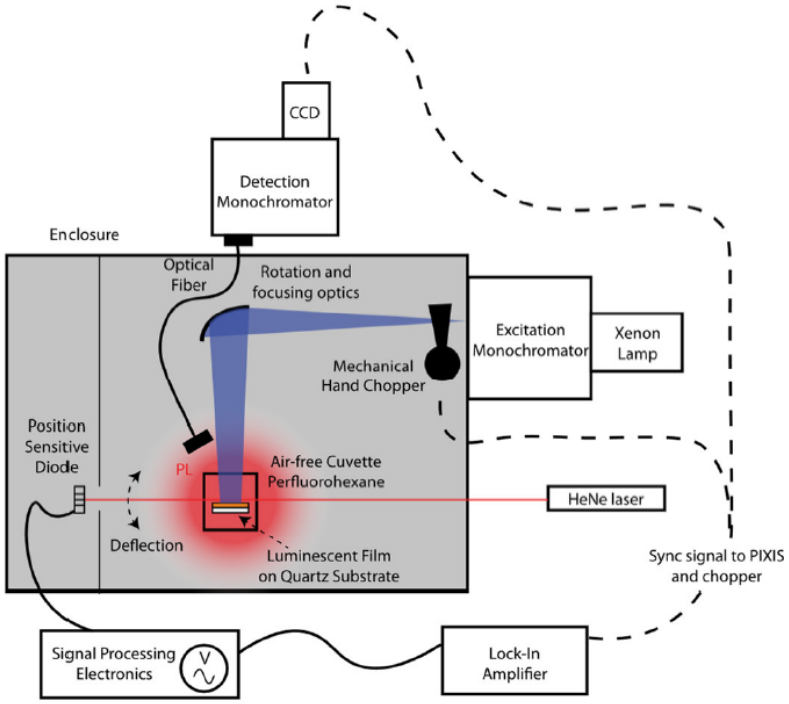

Figure 2.8: A detailed schematic of the PTQY spectrometer provided in Hanifi *et al.*[50]

To explore the physics and chemistry of the near-unity domain requires a method for reliably measuring such small deviations from unity in nanocrystal quantum yields. Conventional measurement techniques of PLQY, which rely on measuring the flux of incident and emitted photons, do not have the necessary accuracy to quantify the photoluminescence efficiency of nanocrystals necessary for the applications of interest here. Previously, the most accurate technique, the integrating sphere method, carried a ~3% error due to sensitivity calibration of detection cameras with a spectral radiance standard[51]. To overcome this, *Hanifi et al.*[50] demonstrated a technique, photothermal threshold quantum yield (PTQY), that measures heat generation from non-radiative processes, thus removing the limitations that arise from reliance on photon flux sensitivity. Breaking this dependency leads to at least an order of magnitude increase in accuracy, opening the door to further exploration of the upper limit of quantum efficiencies.

2.4 Stoichiometric Exploration for Near-Unity $CsPbBr_3$

As discussed in Chapter 1, the $CsPbBr_3$ nanocrystals are inherently defect tolerant due to the ionic nature of the lead-bromide octahedra responsible for the optical transition leading to high as-synthesized PLQY values[52]. The ionic character between the lead and bromide atomic orbitals leads to a reduced depth of electronic trap states associated with undercoordinated surface lead octahedra[53], which have been identified as the most common defects present[54,55]. The electronic states originating from these defects are close to the conduction band or LUMO levels in energy (Figure 2.9). Thus, the light emission arises from a mixed surface and interior energy level that has nearly the same rate for absorption and emission of light as the pristine interior energy level would.

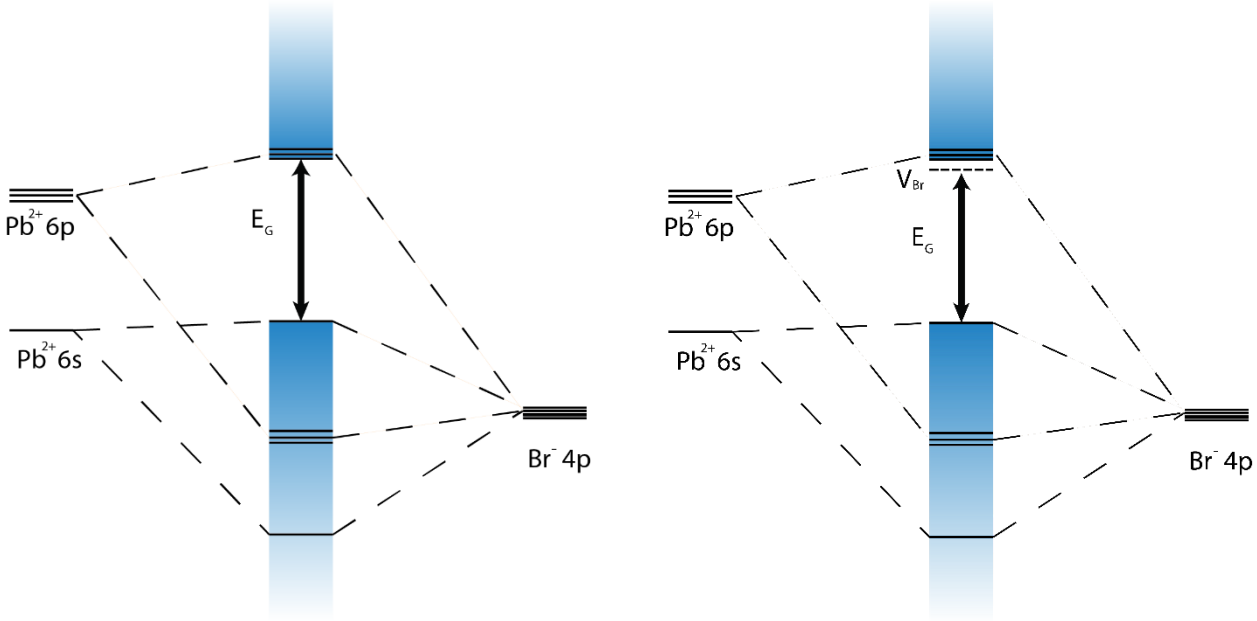

Figure 2.9: The molecular orbital responsible for the optical transition in the $CsPbBr_3$ nanocrystal and the constituent molecular orbitals responsible. The introduction of a bromine vacancy, V_{Br}, produces an electronic trap state within the band gap. However, the ionic nature of the band structure leads to reduced depth of the trap state and a small decrease in optical efficiency.

Nonetheless, undercoordinated Pb atom surface defects will increase the nonradiative rate by a small but non-negligible amount. We estimate that a single such vacancy can reduce the quantum yield from unity to 0.997. Such a difference is undetectable by conventional quantum yield measurement methods. Yet the extremely high PLQY $CsPbBr_3$ system is of interest precisely because it is a suitable candidate material for extremely high quantum yield, and therefore such small differences are worth paying close attention to. Entire classes of new applications can arise when the PLQY asymptotically approaches unity. The most well-known example is laser cooling, which, for the $CsPbBr_3$ nanocrystal system can be reasonably implemented with PLQYs of 0.995 or better[56].

An open question remains: how few under-coordinated Pb surface atoms can be made by established colloidal synthesis methods? To push the luminescence efficiencies to their limits requires a deep understanding of the relationship between synthetic conditions and bromide vacancy formation. Employing ligands to passivate the dangling surface bonds would be the most intuitive approach to reduce the number of electronic trap states within the band gap. While true, the native ligands, oleic acid and oleylamine, have vastly different binding affinities to their respective surface sights. Oleylamine is known to be suitable for passivating cesium vacancies on the surface, while oleic acid is known for its weak binding affinity to lead atoms on the surface hardly filling bromide vacancies[54]. The suppression of bromide vacancies by post-synthetic

treatment is what previously led to PLQY values near unity[54,55]. Since bromide vacancies are undesirable, we can start by imagining a situation where the source of bromide is successively increased in the presence of the colloidal nanocrystals. However, in the original synthetic method developed by *Protesescu et al*.[57], the lead and halide precursor is $PbBr_2$. This leaves a Br:Pb ratio of 2:1. Considering halide-deficient lead atoms at the surface are the main source of defects, this Br:Pb ratio is sub-optimal and provides as-synthesized PLQYs of ~80%.

Indeed, decoupling the Pb and Br precursors has proven useful in increasing the as-synthesized PLQY of $CsPbBr_3$ nanocrystals. Manna et al.[48] accomplished this by using benzoyl bromide as the bromide source and lead acetate as the lead precursor. From this synthesis, it was reported that the as-synthesized PLQY was around ~90% for the $CsPbBr_3$ nanocrystals. Previous work modulating bromide concentration, using oleylammonium bromide[58] or zinc bromide[59,60]. Leveraging the newly decoupled synthesis, a reproducible synthetic method to near-unity quantum yield $CsPbBr_3$ nanocrystals based on an improved understanding of the suppression of surface vacancies in the all inorganic-perovskite nanocrystals. We demonstrate fine control over PLQY and the overall quality of nanocrystals through Br:Pb ratio modulation. While it has been difficult to reproducibly synthesize high PLQY $CsPbBr_3$ due to their rapid growth rate in a hot injection synthesis[57], a highly desirable set of conditions has been discovered through the exploration of concentration adjustments. In addition to the synthetic method, we discuss these alternative phase stabilities at length and establish a critical ratio in which we can exploit the weakly reversible perovskite phase boundaries for high purity, near-unity $CsPbBr_3$ synthesis.

The decoupled synthesis provided by Manna et al.[48] allowed us to survey the synthesis space of the $CsPbBr_3$ nanocrystals. Synthesis of colloidal $CsPbBr_3$ cubes was executed at 8 different Br:Pb ratios, in a ligand-rich environment of oleylamine and oleic acid, to understand how surface halide vacancies would be affected by directly probing their PLQYs optically using an integrating sphere. Each of the 8 synthesis points was repeated 3 times to ensure the reproducibility of the results. These efforts indicate that the optimal Br:Pb ratio is 4.5:1 for the direct synthesis of near-unity perovskite nanocrystals.

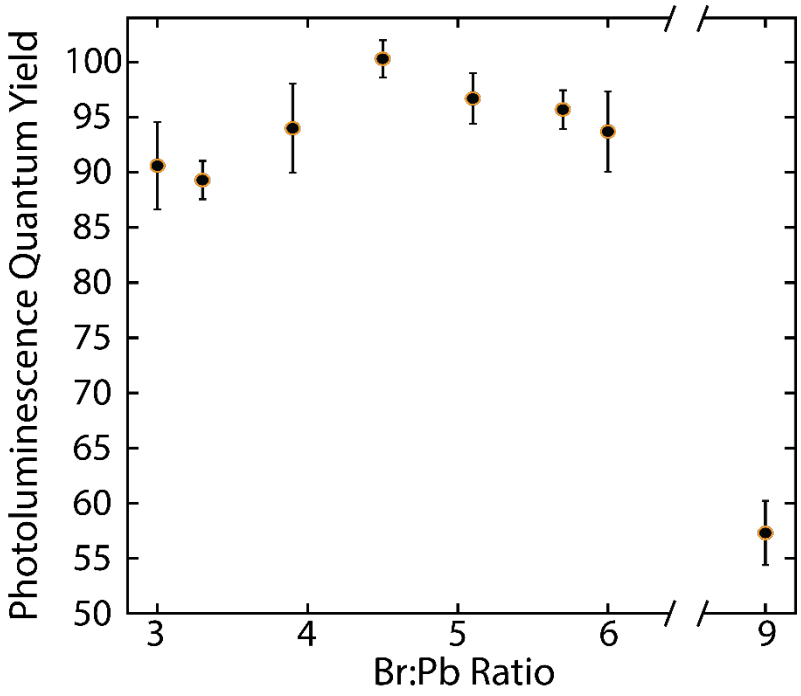

Figure 2.10: Absolute PLQY as a function of the Br:Pb ratio for the CsPbBr3 nanocrystals. Each Br:Pb ratio synthesis was done three times. By increasing the Br:Pb ratio, PLQY increases until the critical ratio of 4.5:1. After the critical Br:Pb ratio, PLQY decreases slowly then a large drop-off is observed at very high ratios.

Intuitively, bromide vacancies should be monotonically suppressed at higher Br:Pb ratios due to the dynamic crystal structure. The quality of the CsPbBr3 nanocrystal surfaces does indeed increase as the bromide concentration in the synthesis increases until the critical 4.5:1 ratio, but then decreases at yet higher ratios (Figure 2.10). Time-resolved photoluminescence (TRPL) comparing the stoichiometric 3:1 to the 4.5:1 Br:Pb (Figure 2.11) displays a clear change in photoluminescent lifetimes. The nanocrystals from the stoichiometric 3:1 Br:Pb synthesis display multiexponential behavior, common amongst semiconductor nanocrystals with defective surfaces[61,62]. In contrast, the nanocrystals from 4.5:1 Br:Pb synthesis display monoexponential decay kinetics more closely aligned with near-unity photoluminescence dynamics. However, if the bromide concentration continues to increase past the optimal 4.5:1 Br:Pb ratio, the PLQY begins to slowly decrease. A steep drop-off was observed at 9:1 Br:Pb where non-radiative processes significantly decrease the PLQY to 57.3% ± 2.9%. If surface halide vacancies were caused by a dynamic equilibrium and the sole contributor to non-radiative recombination, increasing the bromide concentration in the synthesis by any amount should only increase the overall PLQY of the nanocrystals.

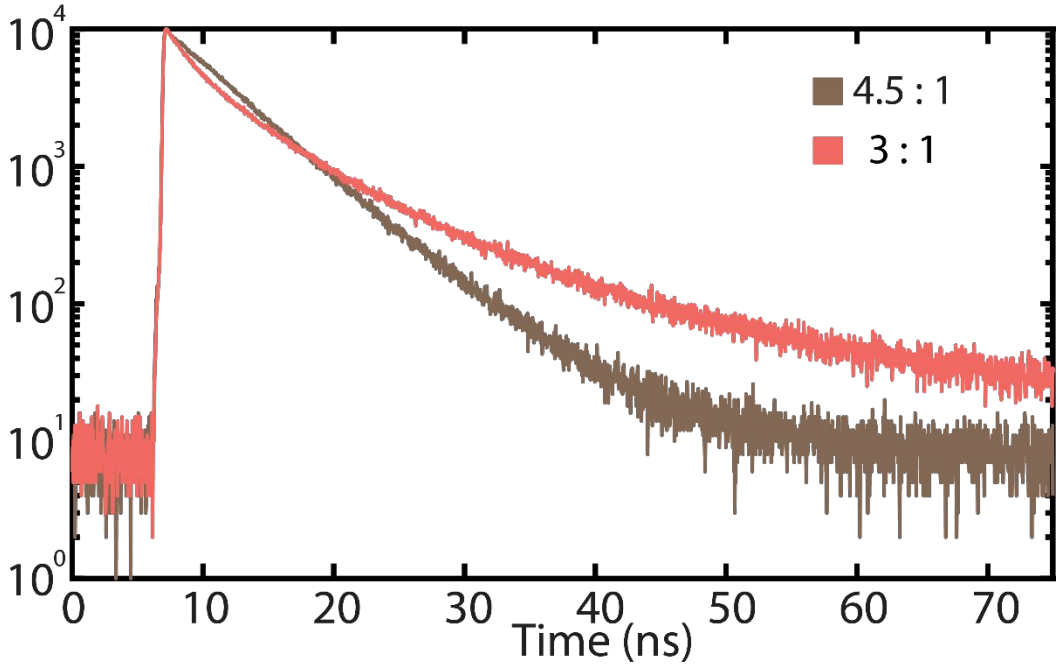

Figure 2.11: Time-resolved photoluminescence lifetimes under pulsed 407 nm excitation for the 3:1 and 4.5:1 Br:Pb ratio CsPbBr3 nanocrystals at room temperature in toluene. The 4.5:1 displays clear monoexponential behavior with a lifetime of 5.32 ns in contrast to the 3:1 which displays multiexponential behavior with a lifetime of 6.52 ns.

Synthetic control over the surface halide vacancies was demonstrated through the exploration of a decoupled lead halide synthetic method which led to a reproducible synthesis of ultra-high quality $CsPbBr_3$ nanocrystals. Undercoordinated lead atoms have been further reinforced as the most detrimental to the optical performance of the $CsPbBr_3$ nanocrystals. A feedback loop between synthesis and measurement of the PLQY allowed for coarse tuning of the synthetic conditions to maximize the quality of the nanocrystals.

By finding the optimal Br:Pb ratio we were able to synthesize CsPbBr3 nanocrystals within error of unity PLQY. Near-unity PLQYs are necessary for unconventional applications such as optical cooling. To successfully cool via anti-stokes photoluminescence (ASPL), upconverted photoluminescent cooling processes must outcompete non-radiative heating. The critical quantum yield of 99.1%, with an upconversion energy of 25 meV, to achieve this cooling is well within the error of the integrating sphere method[56]. To determine if the nanocrystals synthesized by exploiting perovskite phase boundaries are ready for cooling, a more accurate measurement technique must be used to ensure ultra-high quantum efficiencies.

To measure the quantum yield of these nanocrystals with an order of magnitude higher accuracy, we utilized PTQY, similar to efforts in a previous study[50]. Performing these measurements is the only way to determine if the critical quantum yield has been reached and establish a feedback loop between synthesis and characterization in the ultra-high quantum yield region. However, the measurement conditions in the PTQY are harsher than those used for PLQY, which may influence measured outcomes for the dynamic CsPbBr3 nanocrystals with no inorganic shelling as compared to their more stable CdSe-CdS core-shell counterparts. PTQY measurements

are conducted using a thin film of highly concentrated nanocrystals on a quartz slide, and densely packed nanocrystal thin films are known for self-quenching through ultra-fast energy transfer processes[63–65]. These energy transfer processes become much more likely at small interparticle spacings in the film, and the absence of an inorganic shell on the perovskite nanocrystals may lead to a lower minimum distance between absorbing and emitting sites, thus enhancing the self-quenching processes. Additionally, once deposited, the nanocrystals are submerged in perfluorohexane. Perfluorohexane, an inert liquid with a well-defined temperature versus refractive index change, has proven to be detrimental to the nanocrystals in a thin film, and long measurement times inherent with PTQY lead to the degradation of the nanocrystals. Despite the degrading measurement environment, the PTQY of the nanocrystals was determined to be 96.8+/-0.2 (Figure 2.12). This speaks to the quality of the nanocrystals upon synthesis.

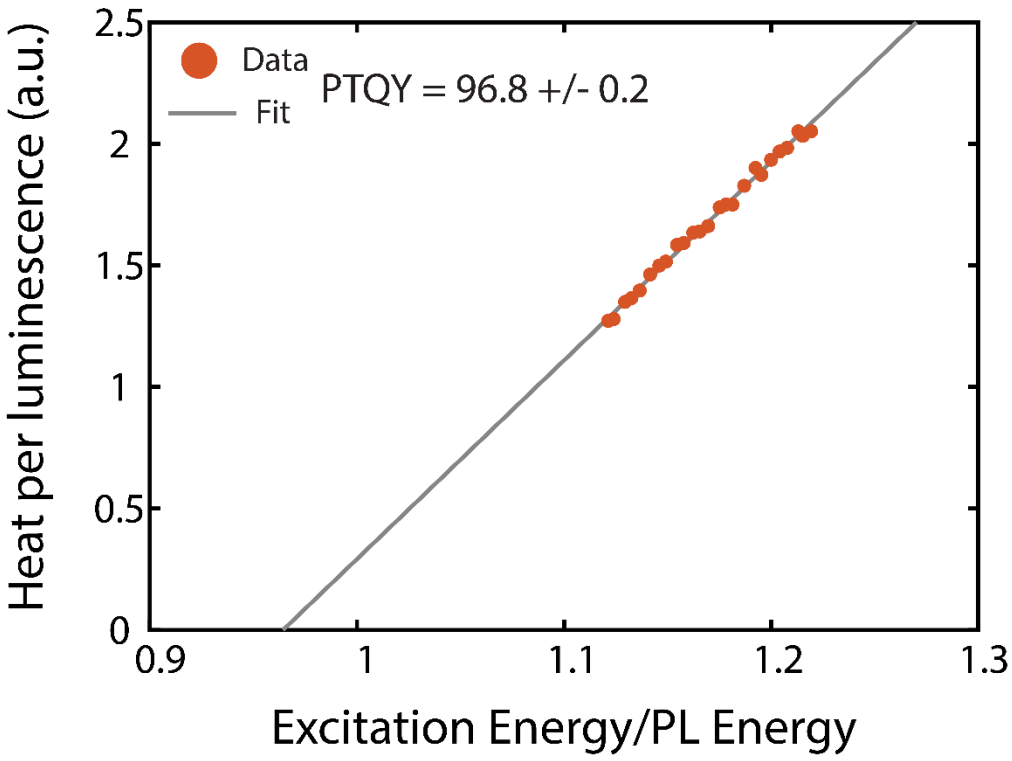

Figure 2.12: Photothermal threshold quantum yield measurement data and fit used to determine the quantum yield of the near-unity quantum yield CsPbBr3 nanocrystals. Self-quenching and degradation of these nanocrystals are likely responsible for the disparity between colloidal quantum yield values (PLQY) and thin-film quantum yield values (PTQY)

Exploration of various encapsulation methods, suspending nanocrystals in a polymer matrix, and atomic layer deposition, proved unsuccessful in maintaining the integrity of the nanocrystals (Figure 2.13). Future endeavors to encapsulate these nanocrystals and improve their stability are necessary to establish a high-accuracy measurement of these near-unity nanocrystals that reflect their true quantum yields.

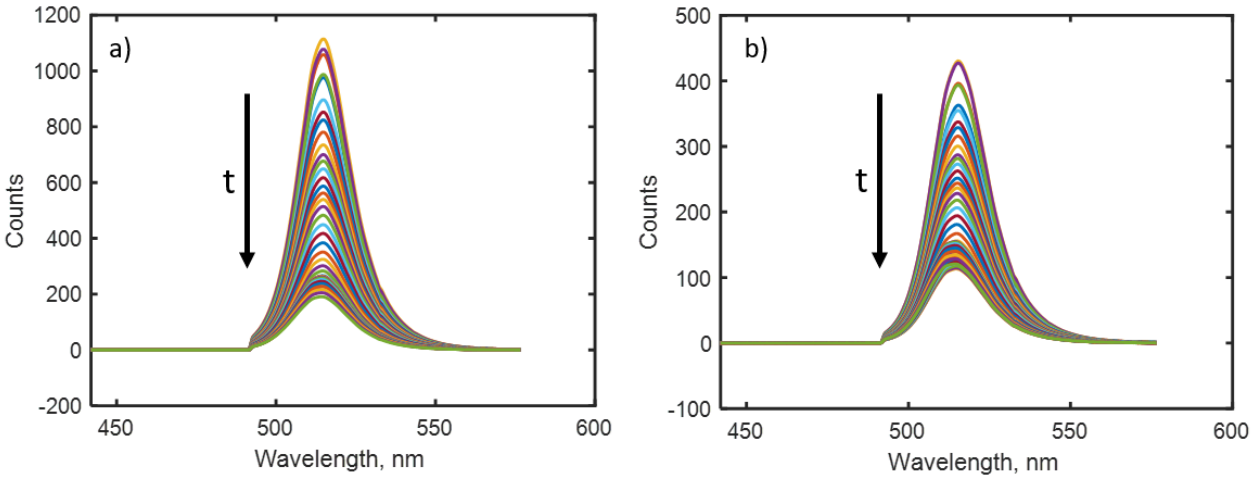

Figure 2.13: Photoluminescence spectra during two encapsulation attempts. (a) Encapsulation in 5 weight percent PMMA. (b) Encapsulation with ALD after drop-casting a film onto the quartz substrate. Both encapsulation methods proved unsuccessful due to the large decrease in PL counts over time. The PL of the nanocrystal film was measured over the course of the 3 hour measurement period every 5 minutes.

In this chapter, we developed a synthetic method toward near unity $CsPbBr_3$ nanocrystals by varying the Br:Pb ratio. A critical ratio of 4.5:1 Br:Pb was determined to be the optimal stoichiometry for the deep suppression of non-radiative recombination. The reproducible nature of this synthesis eliminates the need for post-synthetic treatments that have usually led to The resulting nanocrystals exhibited increased monodispersity from a rigorous size-selective precipitation method and monoexponential decay kinetics often associated with ultra efficient optical systems. Attempts to measure the quantum efficiency with higher resolution were made using the newly developed PTQY instrument. Measuring quantum efficiencies at a higher resolution is critical to the fine tunning of synthetic conditions to reach the thermodynamic limit. Focusing solely on the optical efficiency of the nanocrystals cannot explain the decrease at higher Br:Pb ratios. The decrease in optical performance over the critical ratio due to the complex phase composition of the lead bromide perovskite reaction network will be discussed at length in Chapter 3.

Chapter 3: Phase Transformation of $CsPbBr_3$ and Potential Magic-Sized Clusters

Lead halide perovskites exhibit a rich and complex phase diagram[66], and a variety of nanocrystalline species can be synthesized by adjusting the temperature and concentration of the composite precursors[67–75]. The choice of amine ligand and concentration in the synthesis also significantly influences the selectivity of shapes present[76,77]. The phase boundaries exhibited in this system are often reversible, specifically the $CsPbBr_3$ to Cs_4PbBr_6 phase. The transformation of the desired $CsPbBr_3$ to the lead-depleted Cs_4PbBr_6 is accomplished through the addition of olelyamine[78] while the reverse is accomplished under gentle heating and the addition of oleic acid[79]. The delicate nature of the phase stabilities in this system is critical to understanding the decrease in the PLQY past the critical ratio. The simple picture of bromide ions in equilibrium with the $CsPbBr_3$ nanocrystals does not account for other phase stabilities. Thus, it is important to understand how bromide concentration modulation can affect phase purity as well as quantum yield. Additionally, many applications, such as photovoltaics, require phase-pure nanocrystals to ensure uniform assembly on a substrate, as charge extraction, a necessary feature of photovoltaics, requires close packing of the nanocrystals[80]. In this chapter, we will explore the varying phase stabilities that become present with the modulation of bromine concentration and learn to exploit the phase boundaries associated.

3.1: Phase Modulation in Stoichiometric Exploration of $CsPbBr_3$ Perovskites

The isolated UV-VIS of these nanocrystals (Figure 3.1) across the synthesis space provides a deeper understanding of this system. As the bromide concentration increases beyond the optimal ratio, various phases become more stable such as Cs_4PbBr_6 and the 1 monolayer OLA_2PbBr_4 plate as shown by their characteristic UV-VIS signatures around 315nm and 400 nm respectively. Stoichiometric amounts of lead, cesium, and bromide are removed from the system to form these other phases. It is conceivable that the other phases could scavenge bromide ions; however, at such a high bromide concentration and low $CsPbBr_3$ concentration, there should be excess bromine to passivate the $CsPbBr_3$ being probed. Oleylamine is known to be effective in passivating cesium vacancies on the surface, while oleic acid has a weak binding affinity to lead atoms on the surface and does not effectively fill bromide vacancies[54]. Additional benzoyl bromide reagent could lead to more non-binding amide or acid anhydride side products, but there is a 3-fold excess of oleylamine to Br even at the highest 9:1 Br:Pb ratio. Since the ligand-rich and halide-rich environment provides passivation in the high Br:Pb ratio synthesis, only Pb removal from the system appears chemically reasonable as we move closer to alternative phase boundaries. These lead vacancies in the $CsPbBr_3$ cubic phase will cause larger lattice distortions due to the increase from a monovalent bromide vacancy to a divalent lead vacancy, and result in a deeper trap state than the bromide vacancies[81]. This leads to a steep decrease in PLQY of the $CsPbBr_3$ cubic phase at high Br:Pb ratios.

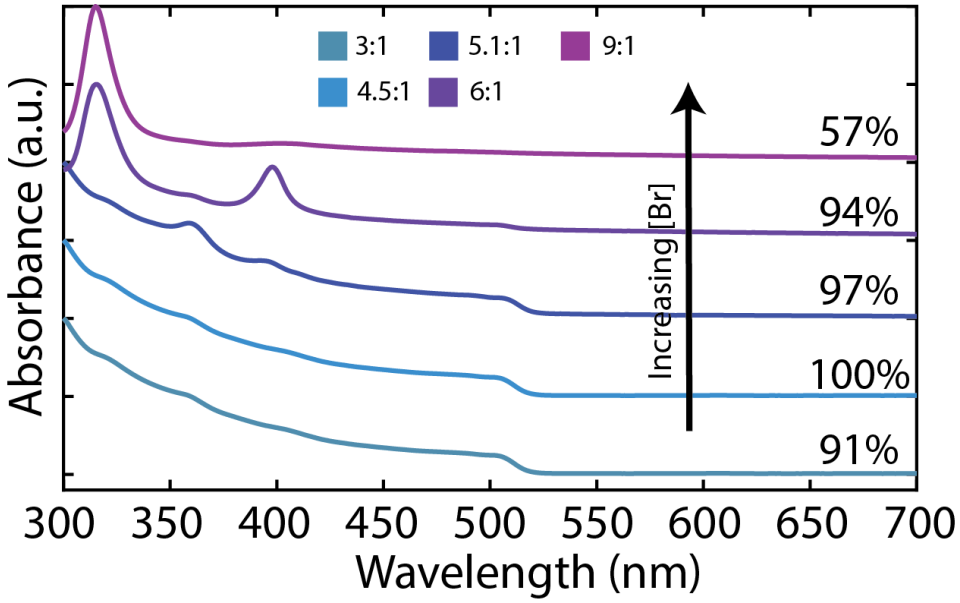

Figure 3.1: UV-VIS of the $CsPbBr_3$ nanocrystals with associated PLQYs. Phase instabilities, indicated by large features in the UV-VIS spectra at 400 nm, 360 nm, and 315 nm, appear as the bromide concentration increases beyond the stoichiometric amount. These peaks are indicative of phase contamination of stabilities other than the desired $CsPbBr_3$ cubes.

To accurately measure the PLQY of the $CsPbBr_3$ cubes, it was crucial to select excitation energies below the range where the alternative phases were absorbing. For consistency between measurements, all samples were excited from 450-500 nm regardless of whether there were alternative phase stabilities present (Figure 3.2). This ensured the probing of the $CsPbBr_3$ phase solely.

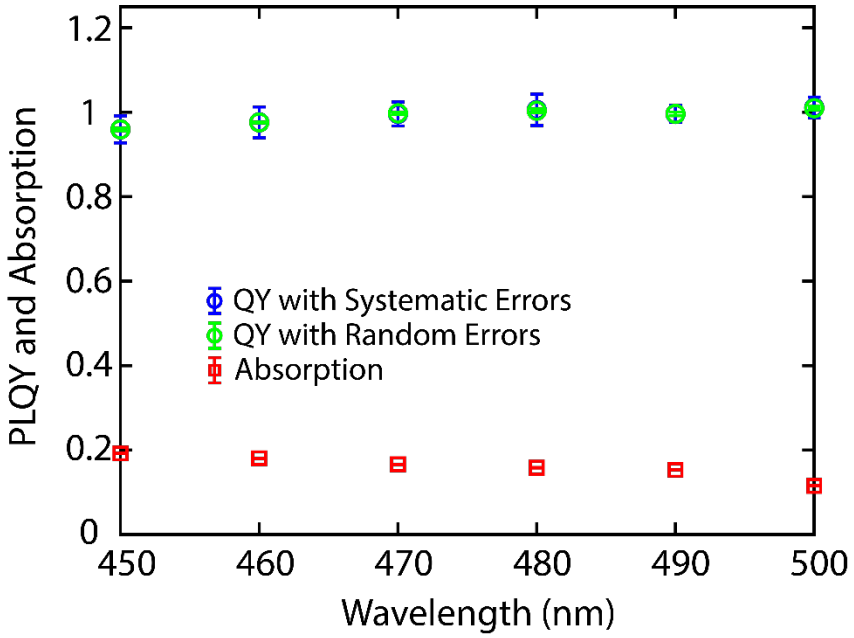

Figure 3.2: A representative PLQY measurement taken from 450 nm to 500 nm with a 10 nm step size. The PLQY value associated with this measurement is 0.99332 $\pm$ 0.020803.

When increasing the Br:Pb ratio, we begin traversing the lead bromide perovskite phase space. Increasing beyond the stoichiometric 3:1 Br:Pb ratio results in other phase stabilities becoming present, although at much smaller concentrations. At ratios past the critical 4.5:1 ratio, alternative phases formed by the excess bromide are largely reduced in concentration in the size-selective precipitation process (Figure 3.3).

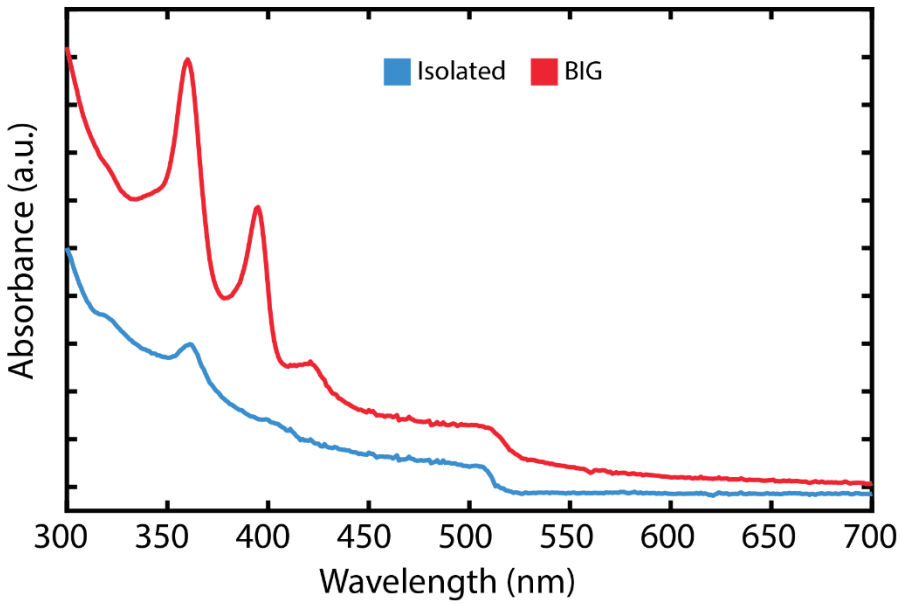

Figure 3.3: The UV-VIS of the isolated vs the big fraction of the 5.5:1 Br:Pb ratio synthesis.

The size-selective precipitation process effectively reduces the concentration of alternative phases in the $CsPbBr_3$ synthesis. In particular, the larger fraction of the size-selective precipitation results in a significant decrease in the concentration of phase instabilities, including the OLA_2PbBr_4 monolayer plates and a 360 nm absorbing species. The OLA2PbBr4 monolayer plates are believed to be removed through a self-assembly mechanism that is often observed for platelets[67,82–84]. When small platelets precipitate out of the solution, they can assemble into larger super-structures, which precipitate out of the solution with the larger particles. Phase instabilities in the samples far above the optimal ratio are at such a high concentration that they cannot be removed even when employing the size-selective precipitation method. This is seen in the isolated absorption spectra of these nanocrystals that retain characteristic UV-VIS peaks of alternative phases. Overall, the successful removal of these alternative phases through size-selective precipitation is an important step toward obtaining pure and high-quality CsPbBr3 cubes for various applications.

A similar type of optimal point was found for CsPbBr3 nanoplates and nanocubes based on data from a high-throughput synthesis campaign[85]. The relative quantum yield measured in this system as a function of the Br:Pb ratio showed an optimum at a ~3:1 Br:Pb ratio as derived from the entire dataset[66] (Figure 3.4). The 3:1 Br:Pb ratio is significantly lower than the 4.5:1 ratio determined for the CsPbBr3, which could be due to the reduction in temperature by over 100 °C or the reduction of oleylamine concentration. Either of these could cause tighter binding of the bromide to the surface, in addition to the change from nanocube to nanoplatelet. What remains the same is the type of change: at low Br:Pb ratios, the phase purity is high while the relative quantum yield is lower. Once the Br:Pb ratio passes the optimum point, phase purity decreases alongside the quantum yield. These results further demonstrate that during synthesis, increasing bromide precursor concentration is only beneficial to the quantum yield up to a certain point, after which the quantum yield decreases.

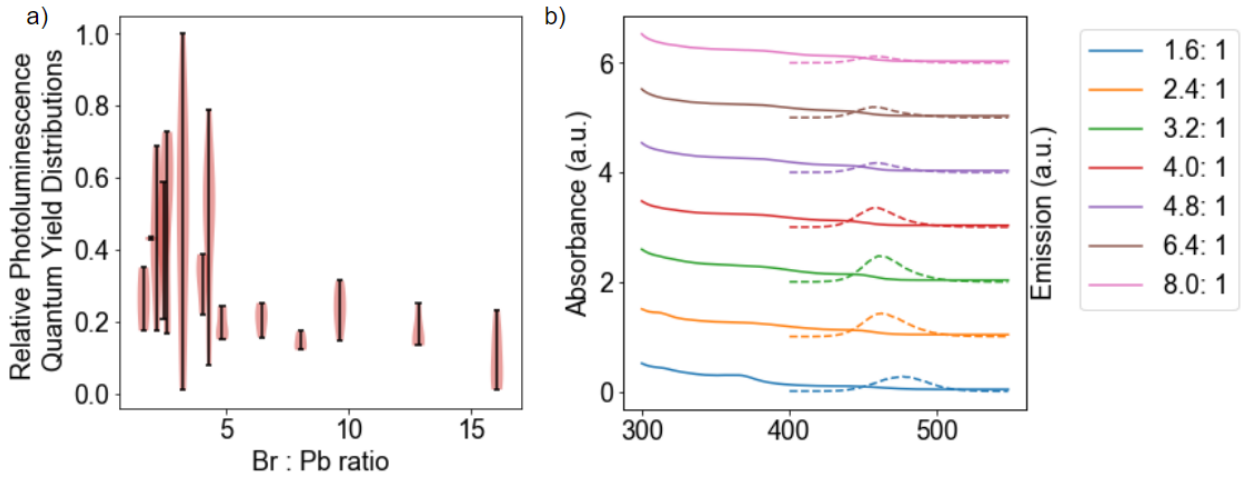

Figure 3.4: (a) Displays the range of photoluminescence quantum yields measured for the nanoplates and nanocubes at varying Br:Pb ratios. (b) Absorbance (solid) and photoluminescence (PL) for varying Br:Pb ratios on this high throughput campaign.

The lead bromide perovskite system has a rich and complex phase diagram with various phases present at different compositions and temperatures. By careful investigation and analysis, we identified a critical ratio, which is a unique composition of the precursor solution that lies at the phase boundary and yields high-quality and phase pure CsPbBr3 cubes. This critical ratio is a result of the interplay between the solubility of the precursors and the formation of different phases during the reaction process. By exploiting this critical ratio, we were able to precisely control the synthesis conditions to produce ultra-high quality CsPbBr3 cubes. The discovery of this critical ratio represents a significant step toward a deeper understanding of the lead bromide perovskite synthesis and paves the way for the development of high-performance optoelectronic devices. With this deeper understanding of the change in phase stabilites over the stoichiometric space, the Br:Pb ratio vs PLQY graph (Figure 2.10) can be more comprehensive. Including the phase stabilities and defects present (Figure 3.5).

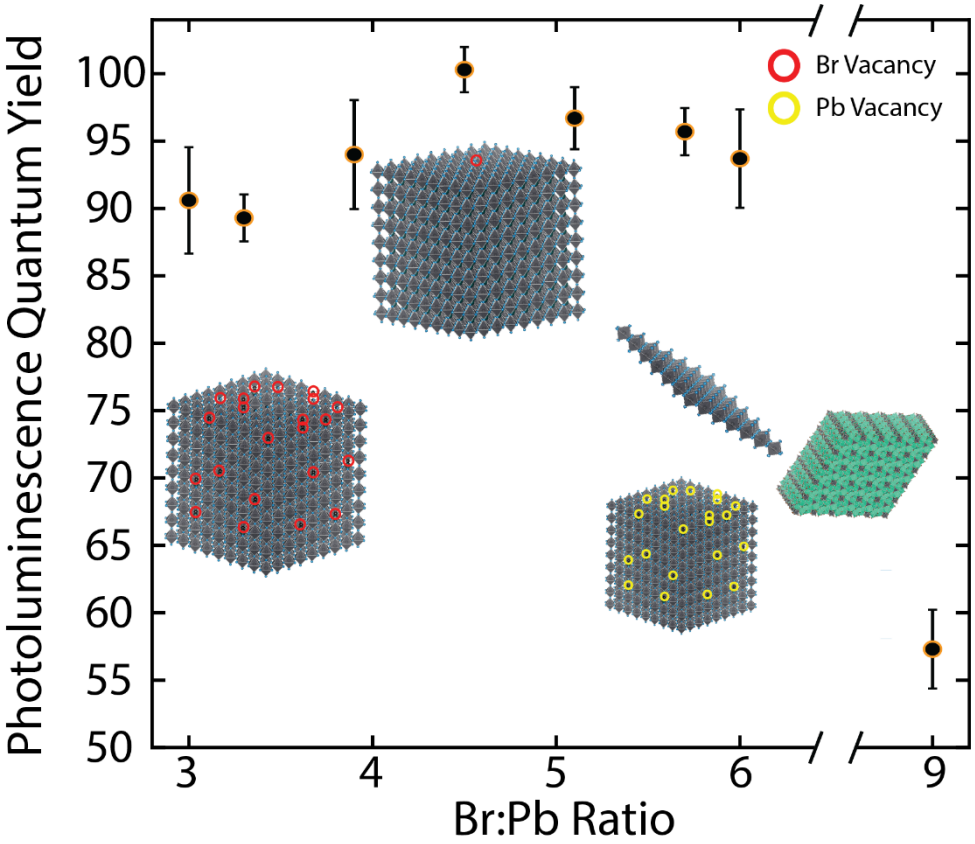

Figure 3.5: The Br:Pb ratio vs PLQY of the nanocrystals including the phase stabilities and the defects present in the $CsPbBr_3$ cubes. After the critical ratio, 4.5:1, the 1 ML plate and Cs_4PbBr_6 phases become more stable and are deleterious to the optical performance of the $CsPbBr_3$ cubes.

3.2: Investigation of Lead Bromide Precursor of Larger Lead Bromide Perovskites

By systematically exploring the lead bromide perovskite phase space, we successfully identified the alternative phases that coexist with the desired $CsPbBr_3$ cube phase. However, a 360

nm absorbing species remained unidentified. This species is commonly observed as a contaminant in UV-VIS spectra reported in the literature[86–88] yet never addressed. When synthesizing the $CsPbBr_3$ cubes at higher Br:Pb ratios, the 360 nm species would become present. By leaving the diluted sample used to take UV-VIS out for 24 hours, we were able to determine that the 360 nm absorbing phase is transient and is transformed into platelet species (Figure 3.6).

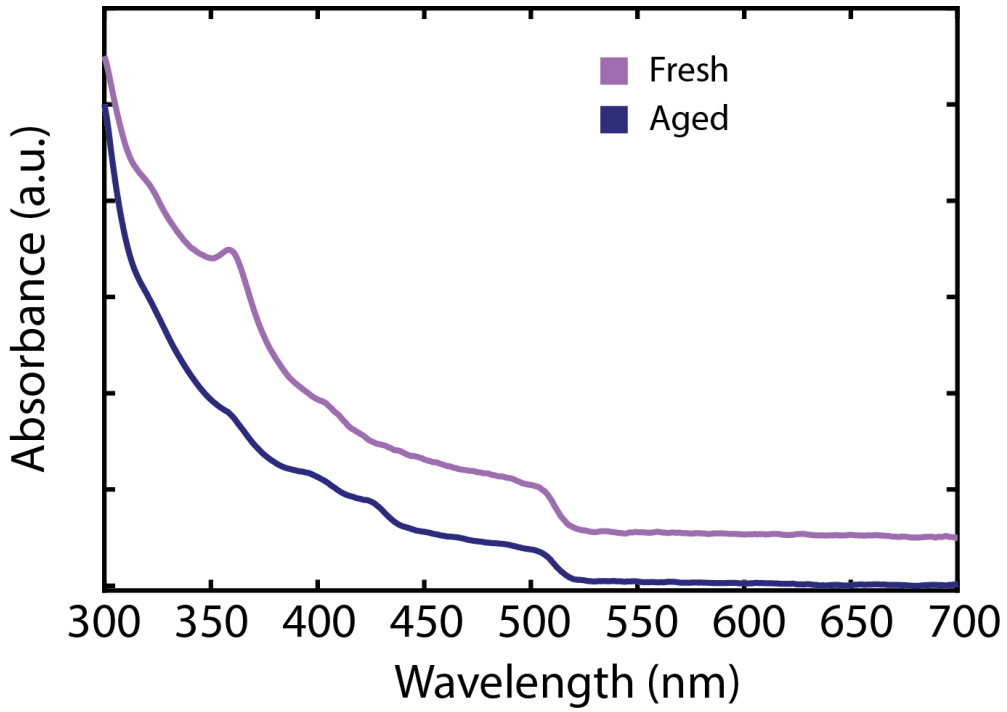

Figure 3.6: UV-VIS spectra of a fresh vs aged $CsPbBr_3$ synthesis contaminated with the 360 nm absorbing species. The fresh spectrum shows a characteristic peak at 360 nm The aged spectrum shows a decrease in the 360 nm peak and a growth of a peak around 430 nm commonly associated with the $OLA_2CsPb_2Br_7$ 2 monolayer platelet.

Due to its transient nature, characterizing and investigating this species was difficult. Therefore, isolating the species was essential to identifying its chemical and physical properties accurately. Once isolated through a high throughput synthesis campaign provided by Dahl *et al.*[85], a deeper understanding of the transformation pathway and identity of the species was gained. The identification of the species provides valuable insight into the formation mechanism of the lead halide perovskites. Probing the chemical transformations of these transient species is essential to furthering precise control over the synthetic conditions that facilitate high-quality nanocrystals.

Synthesis of 360 nm Absorbing Species: In a 3 mL glass vial with a stir bar, 120 µL of oleylamine and 90 µL of oleic acid, were added to 2 mL of hexane. After stirring briefly, 30 µL of a 0.5 M lead oleate solution and 8 µL of benzoyl bromide were added. The solution was temporarily a white milky color but almost instantaneously became transparent after stirring. After 5 minutes, 10 µL

of the solution was diluted into 3 mL of hexane in a quartz cuvette for UV-VIS spectroscopy. A signature peak around 360 nm was indicative of a successful synthesis.

The UV-VIS spectrum of synthesized species contained the characteristic 360 nm peak. Probing how the lead bromide species transforms upon the introduction of cesium provides valuable insights into the formation of cesium lead halide nanocrystals. By carefully monitoring the transformation pathway and identifying intermediate species, we can better understand the factors that govern crystal nucleation and growth. To initiate the transformation of the lead bromide species, varying equivalents of a 0.5 M cesium oleate solution were titrated into the 3mL glass vial and stirred. Similarly, after 5 minutes of stirring, 10 µL of the solution was diluted into 3mL of hexane in a quartz cuvette UV/VIS spectroscopy (Figure 3.7).

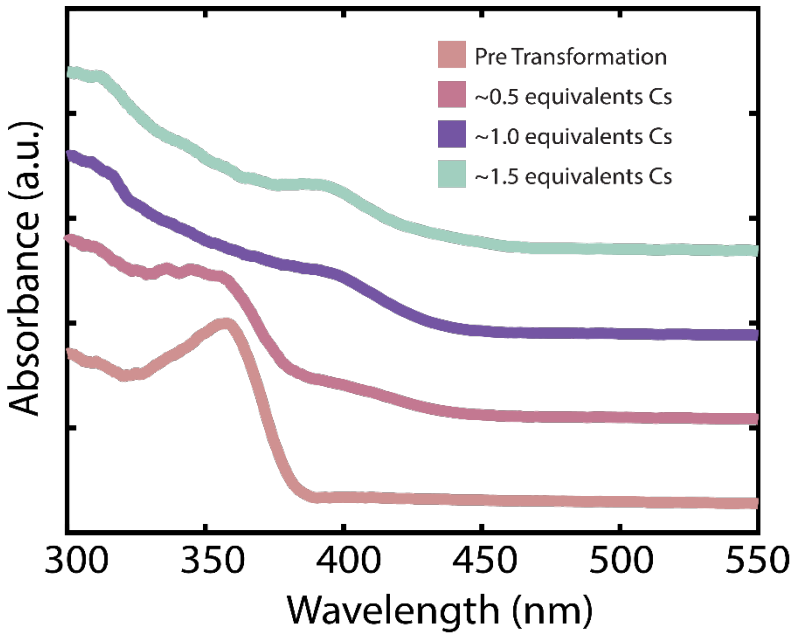

Figure 3.7: UV-VIS spectra of the isolated lead bromide species before and after adding varying equivalents of cesium.

Upon excitation with a UV LED, a notable blue photoluminescence was observed in the diluted solution. Characterizing the photoluminescence and the photoluminescence excitation (PLE) of the species was essential to determine the electronic properties of the species (Figure 3.8). The spectra were taken immediately after the transformation. The transformed species has a photoluminescence centered around 470 nm. A significant difference between the absorbance and the PLE spectra is observed. This implies a pseudo-breaking of Kasha's rule and suggests alternative pathways for deexcitation than relaxation from the ground state.

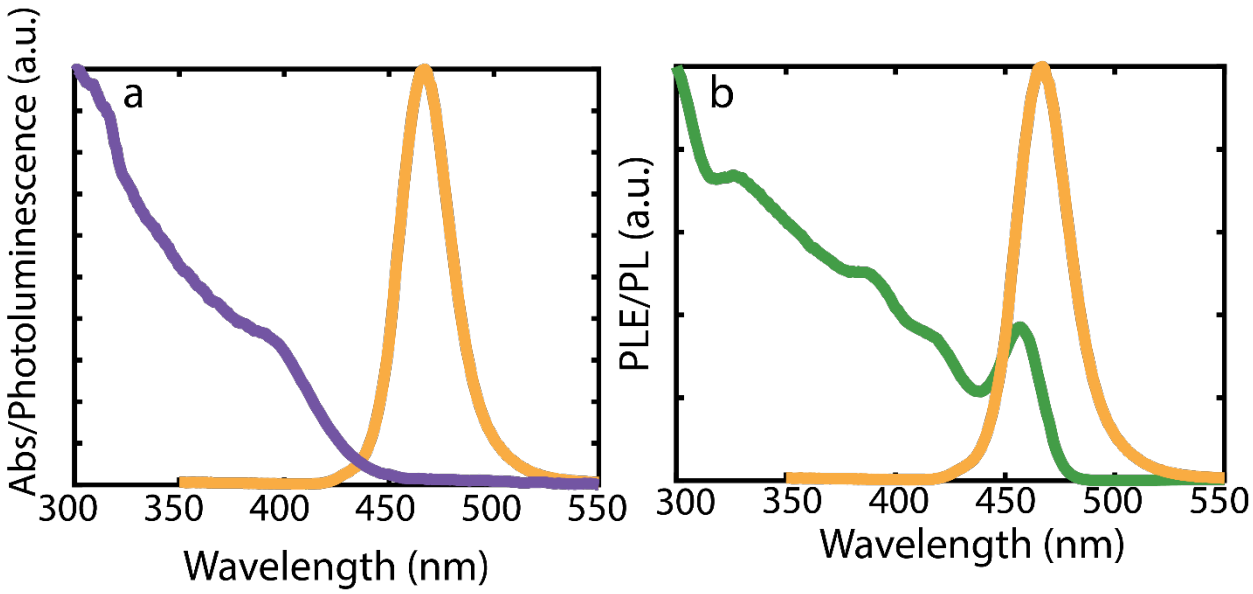

Figure 3.8: a) UV-VIS and photoluminescence spectra of the transformed species at 1 equivalent of cesium. b) Photoluminescence and photoluminescence excitation spectra of the transformed species

Of particular importance, the concentrated stock solution that the 360 nm species were synthesized in did not exhibit the same blue photoluminescence hence implying that little to no transformation occurs. This parallels previous observations of the 360 nm species contaminating the $CsPbBr_3$ cubes. The species is incredibly stable when in its concentrated form, even with excess cesium present. Only upon dilution does the species transform. This suggests that the transformation between species is ligand-mediated. As the sample becomes diluted, the ratio between the ligands bound to the species and free ligands in the solution decreases. The formation of the luminescent species presented above is likely attributed to the aggregation of small monomers with free cesium, which has been observed in the literature as an aggregation of pseudo magic-sized clusters[89]. The aggregation process is likely facilitated by weak interparticle interactions and the extent to which the 360 nm absorbing species transforms is dependent on the total free cesium in the solution (Figure 3.7). The aggregation of magic-sized clusters to form larger species is observed in many of the prototypical nanocrystalline systems[90,91].

The transformation from these magic-sized clusters to the 470 nm luminescent species provides a snapshot in the formation of larger lead halide perovskite nanocrystals. Further characterization of the transformed species proved difficult due to its transient nature. Upon aging, the intermediate 470 nm luminescent species further transforms into larger lead bromide perovskite structures (Figure 3.9). Specifically, after just 5 minutes of aging, the transformed species forms Cs_4PbBr_6, $CsPbBr_3$, and $OLA_2CsPb_2Br_7$ 2 ML plates identified via their characteristic UV-VIS signatures. The 470 nm luminescent species is likey an intermediate between the magic-sized clusters and the larger lead halide perovskite phases.

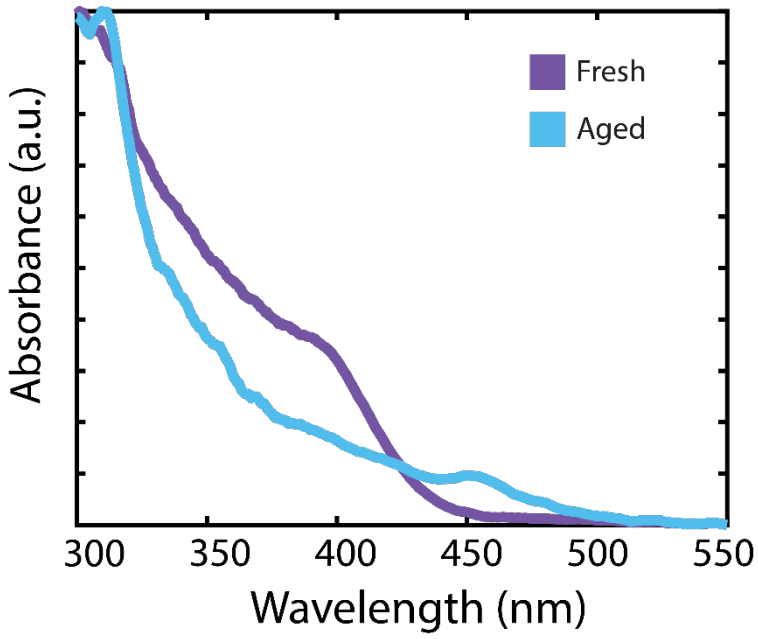

Figure 3.9: UV-VIS spectra of the fresh vs aged transformed species at 1 equivalence of Cs. Clear UV-VIS signatures of Cs_4PbBr_6, $CsPbBr_3$ and $OLA_2CsPb_2Br_7$ 2 ML plates are present.

The formation of the larger lead halide perovskites from these magic-sized clusters is caused by particle-particle aggregation with an transiently stable, weakly luminescent intermediate species. Aggregation of these particles under dilute conditions implies a ligand-mediated growth process. The proposed mechanism of formation for lead halide perovskites (Figure 3.10) follows closely with the previous observation of lead halide perovskite nanoclusters transformation into larger species[89].

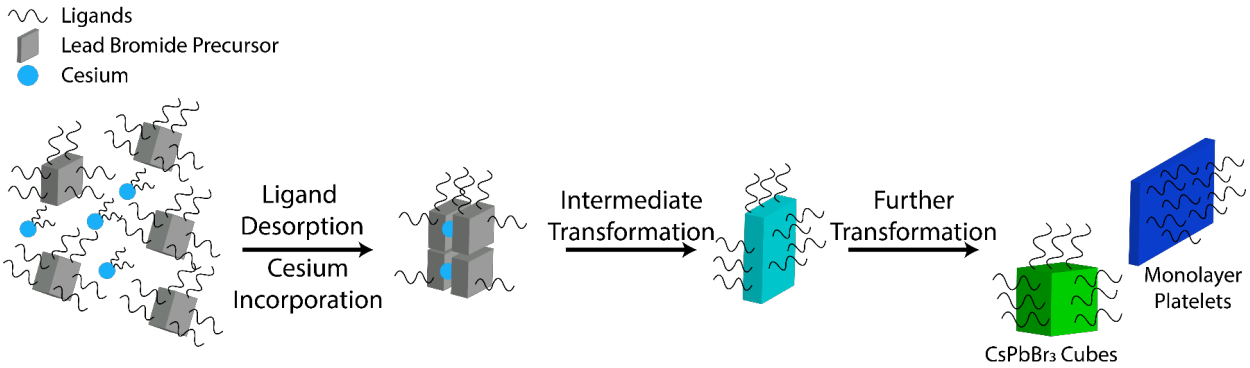

Figure 3.10: Proposed mechanism of formation of lead halide perovskites based on experiments provided. Transformation from magic sized clusters to intermediate species is accomplished via ligand desorption from the lead bromide precursor and incorporation of cesium. Further transformation likely follows a similar mechanism of particle-particle aggregation into larger lead bromide perovskites

Understanding the fundamental formation mechanism of the lead halide perovskite can shed light on potential areas for synthetic optimization for the design of higher-quality materials. We believe that challenges of monodispersity and precise phase control can be overcome by exploring the nature of lead halide magic-sized clusters. A deeper understanding of the initial ligand desorption and cesium incorporation are essential to controlling the quality of the intermiediate species. Identyifying the size, phase, and electronic properties of the intermediate species is critical. Stability challenges may be overcome by doing transformations at high ligand concentrations to prevent the self-assembly into larger lead halide species. Developing a comprehensive understanding of the mechanism responsible for the secondary transformation is the key to unlocking control over the formation of larger lead bromide perovskite species.

In this chapter, we discussed the complex and rich phase diagram of the lead bromide perovksites and how it plays a role in the stoichiometric enchancement of the $CsPbBr_3$ cubes. By understanding the role of the various phase stabilities in the synthesis of lead bromide perovskites, we were able to exploit the delicate phase boundaries to synthesize high quality nanocrystals. We also explored beyond the phase boundaries and hypothesized a potential defect responsible for the decrease of PLQY at high Br:Pb ratios. The use of these near unity PLQY nanocrystals in devices could boost their efficiencies. In the next chapter, we will explore the the inter-nanocrystal coupling of these nanocrystals by probing their exciton diffusion lengths in a 2D nanocrystal array.

Chapter 4: Probing the Inter-Nanocrystal Coupling in 2D Array of $CsPbBr_3$ Nanocrystals

By measuring the diffusion lengths of excitons and fluorescent lifetimes in thin films of these high quality nanocrystals, we can extract the diffusivity of the energy transfer system. The measurement of exciton diffusion was previously done by *Penzo et al.*[92] and determined to have a diffusion length of ~200 nm and a diffusivity of 0.5 cm^2/s at room temperature. The diffusion lengths were uncharacteristically high as prototypical nanocrystal solids have diffusion lengths of ~30-100 nm[93–95]. The high diffusion lengths are likely attributed to the $CsPbBr_3$ nanocrystals' high-monodispersity, efficient packing, and possible inter-nanocrystal coupling. Self-assembly of perovskite nanocrystals into larger superstructures has been proven to increase inter-nanocrystal coupling[96,97], and signatures of increased coupling in 2D films of $CsPbBr_3$ nanocrystals has been observed[98,99]. Controlled evaporation of highly monodisperse $CsPbBr_3$ nanocrystals resulted in highly ordered domains of nanocrystals in these superstructures. The small interparticle distance and ordered orientation of transition dipoles of the nanocrystals results in strong coupling between them. Under sufficiently strong coupling between quantum dots, excitons can become delocalized across multiple quantum dots, resulting in a superposition of the individual quantum dot wave functions. Recently, superradiance, a direct result of the delocalization of excitons over multiple quantum dots, has been shown in these super lattices[100].

The formation of super lattices to promote the coupling between quantum dots is a delicate process that usually involves the slow and controlled evaporation of a solvent, containing the quantum dots, on a substrate. It is unlikely that the benefits of exciton delocalization can be utilized in optoelectronic applications due to the high-throughput fabrication of devices. Maintaining the high coupling between quantum dots while reducing the dimensionality of superlattices can be achieved more easily by spin-coating nanocrystals onto a substrate, which may be a desirable approach. To determine if strong coupling between the nanocrystals is occuring in these 2D monolayers, temperature dependent exciton diffusion and time-resolved photoluminescence can be conducted to extract the diffusivity. In incoherent systems, the diffusivity should follow Arrhenius-like behavior upon a change in temperature[101]. In coherent systems, the diffusivity should reflect the opposite trend with a change in temperature due to the loss of coherence given an increase in phonon scattering in the system[102].

4.1: Experimental Method

Hydrocarbon Substrate Functionalization: A hydrocarbon layer was deposited in an Oxford Instruments PlasmaLab 150 inductively coupled plasma etcher. Samples were first cleaned in an oxygen plasma (O2 60 sccm, 30 mTorr, 100 W), followed by methane polymerization (CH_4 20 sccm, 40 mTorr, 100 W, 10 ^oC) to obtain a thickness of 12 nm. Polymer thickness was estimated using the J.A. Woollam M-2000 spectroscopic ellipsometer by fitting the obtained data with a Tauc-Lorenz model. The deposition rate was extracted to be 6 nm/min. Detailed outline of this method can be found in Penzo *et al.*[92]

Monolayer Sample Fabrication: Following the synthetic method described in Chapter 2, the isolated $CsPbBr_3$ nanocrystals were diluted down to ~1 μM in concentration. This concentration was found to give a long range, ordered single monolayer of $CsPbBr_3$ nanocrystals. All samples were prepared by spin coating onto a silicon wafer coated with 12 nm of a -CH terminated polymer at 1500 rpm for 60 seconds. To ensure stability all spincoating was done in an inert atmosphere glovebox.

To ensure an even monolayer of nanocrystals, it is essential to functionalizing the surface with the -CH terminated polymer. Van der Waals forces between the surface polymer and the ligands on the nanocrystal's surface facilitate even monolayer formation over long ranges (Figure 4.1b). Without the -CH terminated polymer, the nanocrystals aggregated into larger structures (Figure 4.1a). After functionalizing the surface, small adjustments to the concentration and spin coating speed can be made to fine tune the monolayer formation.

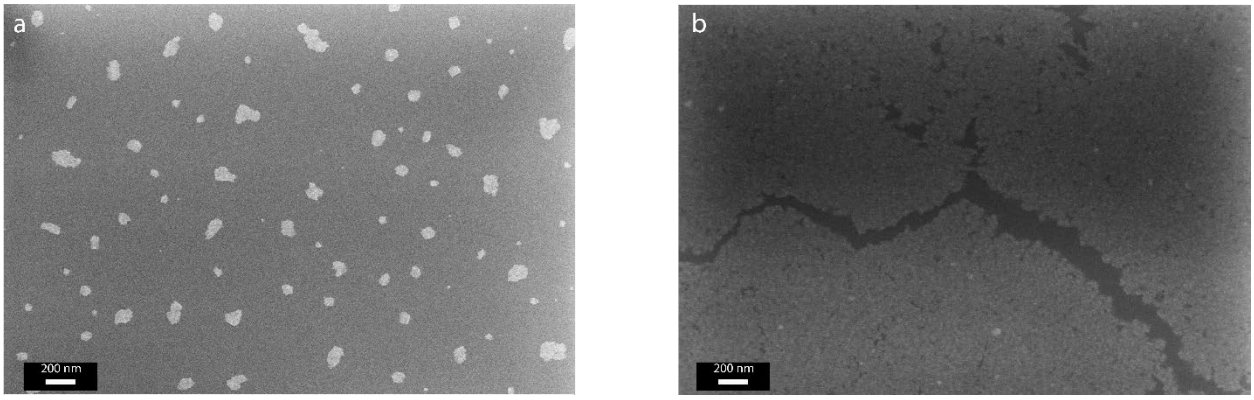

Figure 4.1: SEM photos of the (a) unfunctionalized versus (b) the functionalized substrates with nanocrystals spin coated on them.

Exciton Diffusion Measurement: These measurements were carried out using a Montana Cryostation s200 close-cycle helium cryostat with fine temperature control from 5 K to room temperature and a 100x optical magnification. Specifically, we measured the exciton diffusion of the perovskite nanocrystals from 5 K to 265 K every 20 K. To ensure stability of the nanocrystals and condensation of contaminants did not occur, the sample chamber was held at $1x10^{-6}$ Torr. The samples were excited using a pulsed (38.9 MHz) supercontinuum laser tuned to 450 nm with a 5 nm linewidth. Real space imaging of the photoluminescence was achieved using a CMOS detector in a time integrated detection mode. Longpass or shortpass filters were utilized to remove the laser or PL to acquire separate images. To acquire spectral resolution of the photoluminescence, a Peltier-cooled CCD through a detection spectrometer with a 300 lines/mm grating. Each steady-state PL measurement was integrated for 10s. To acquire time-resolved PL spectra, the nanocrystal emission was outcoupled to an single photon counting avalanche photodiode connected to a time-correlated single photon counting unit (Picoharp 300). A schematic of the home-built setup is below (Figure 4.2)

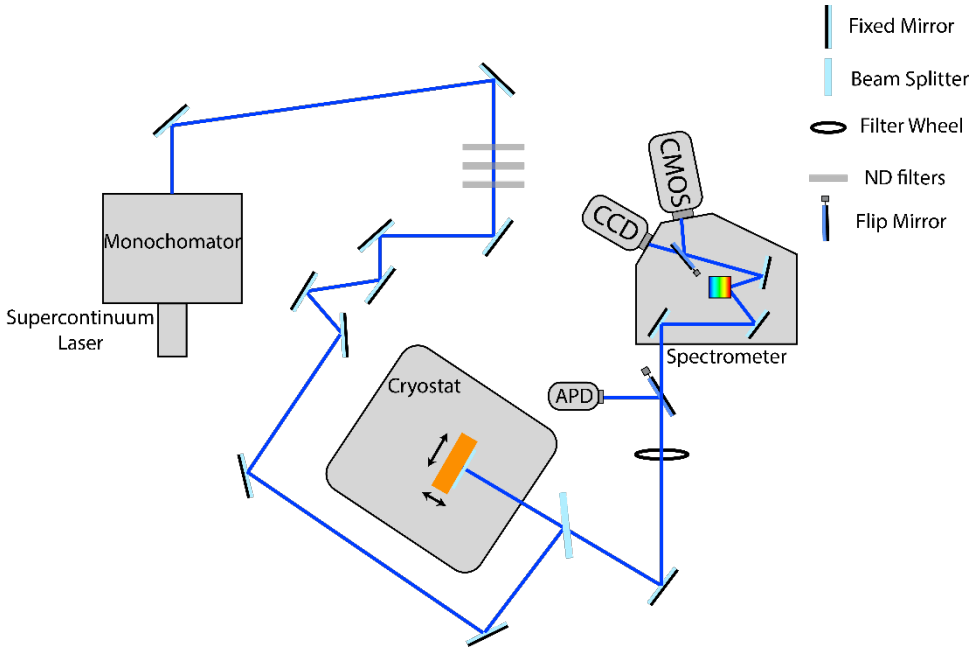

Figure 4.2: A schematic of the home-built exciton diffusion setup using the Montana cryostat for fine temperature control

4.2 Temperature Dependent Exciton Diffusion and TRPL

Real space imaging of the photoluminescence using the CMOS detector allowed for deconvolution of the Gaussian distribution fitted to both the photoluminescnence and the laser spot (Figure 4.3). The diffusion length of is defined by:

$$L = \sqrt{\sigma^2 - \sigma_L^2} \tag{4.1}$$

Where σ_L is the gaussian variance of the laser intensity and σ is the gaussian variance of the real space photoluminescence intensity, both centrocymetrically evaluated along an arbitrary axis (Figure 4.3). The diffusion length is calculated as the square root of the difference between the squared variances.

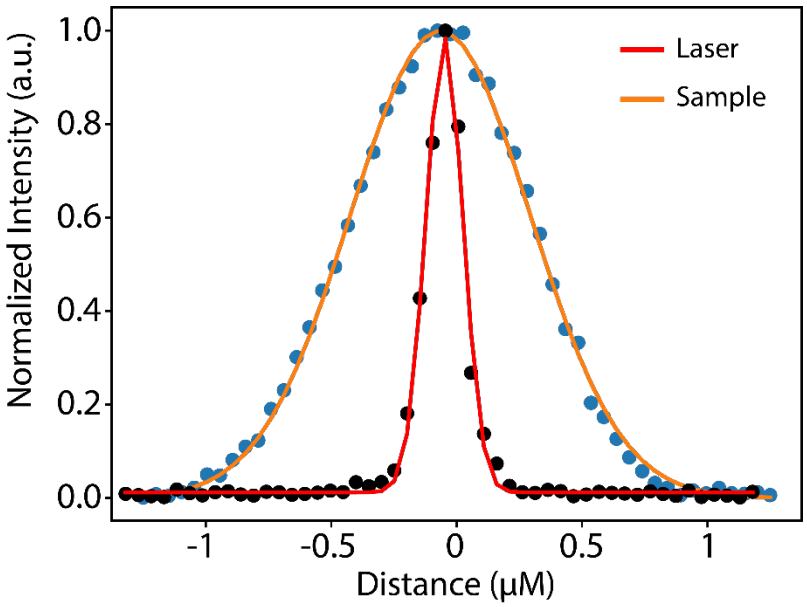

Figure 4.3: Guassian fit of both the laser and the photoluminescence from the sample. A clear broadening associated with diffusion of the exciton through the film is seen here.

By fitting the laser and the photoluminescence to a gaussian function from the sample at each temperature, we are able to determine the diffusion length (Figure 4.4).

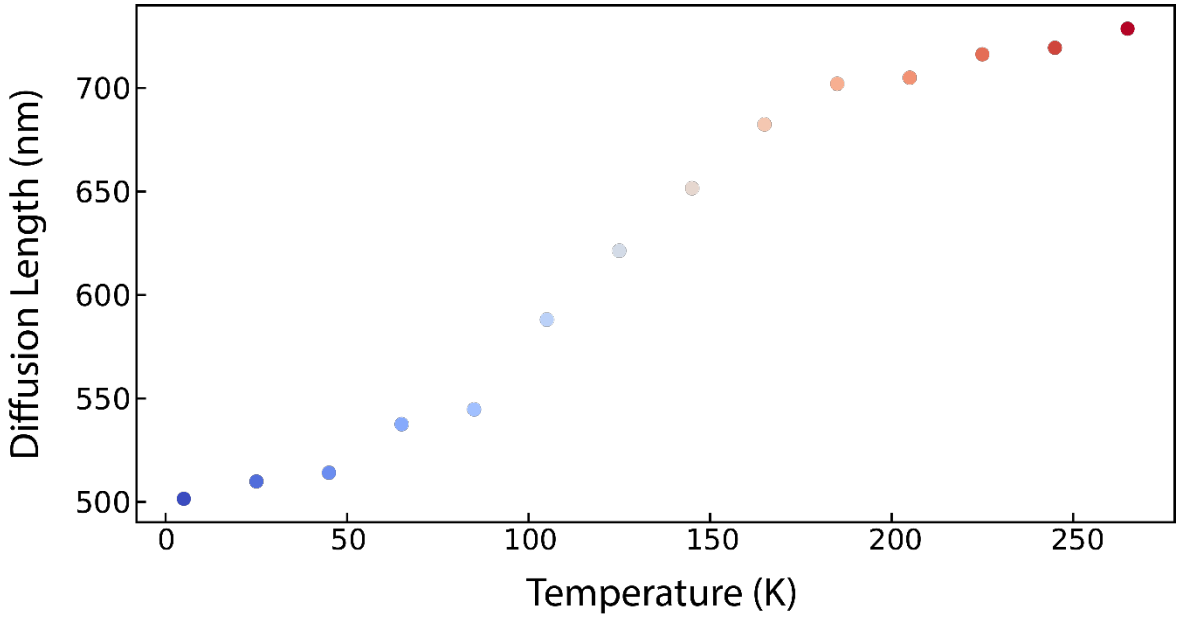

Figure 4.4: The diffusion length of the $CsPbBr_3$ films vs the temperature in Kelvin

An increase in the diffusion length of the 2D array of $CsPbBr_3$ nanocrystals is logical since the thermal activation of the exciton hopping increases with temperature. Excitions are able to overcome energetic disorder arising from variation in quantum dot size within the ensemble as the thermal energy of the system increases. This follows closely with the effects of inhomogenous

broadening in disordered organic materials[103]. Diffusion lengths found were much larger than previously found by *Penzo et al.* This is likely due to the rigorous encapsulation method used to prevent degradation of the quantum dots while exposed to ambient conditions. The utilization of atomic layer deposition for depositing alumina onto $CsPbBr_3$ thin films has been demonstrated to reduce the diffusion of excitons [104]. Due to the high vacuum achieved in the Montana cryostat, we were able to avoid encapsulation and prevent the degradation of the nanocrystals. We also employ a comprehensive size-selective precipitation method to reduce the size distribution of the nanocrystals (Chapter 2). An overall reduction in the size distribution results in the suppression of inhomogeneous broadening of the ensemble.

The diffusion length of the excitons in the system at different temperatures is inadequate to probe the coherence of the film of nanocrystals. To do this, the fluorescent lifetime, τ, must be determined via time-resolved photoluminescence. Thus, time-resolved photoluminescence was also measured at each temperature (Figure 4.5a).

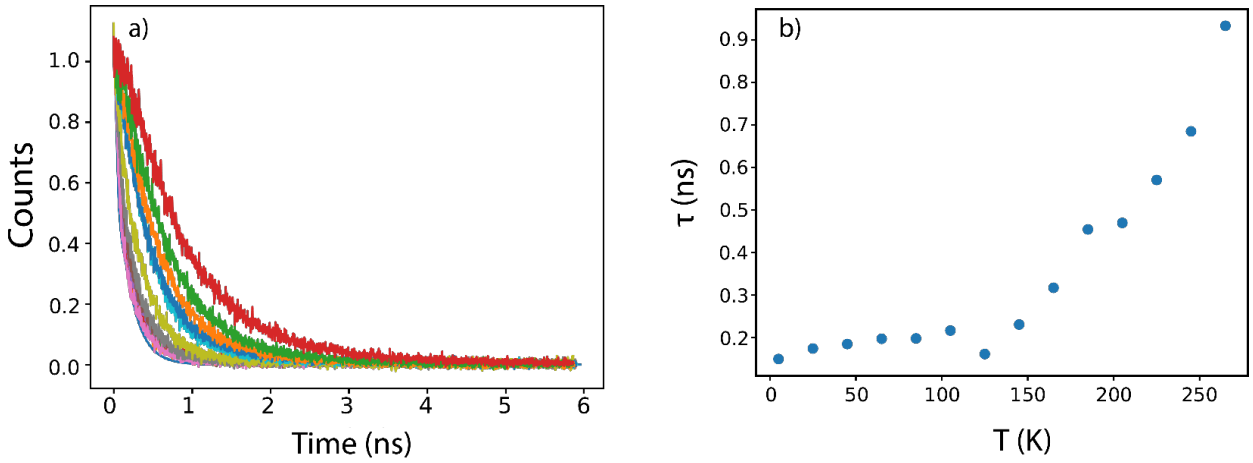

Figure 4.5: (a) The time resolved photolumiscence decays at varying temerpatures, with the peak counts set at time zero, and (b) the extracted lifetimes plotted vs temperature. Although the fitting has associated error bars, they are too small to be displayed.

By measuring the decay kinetics at each temperature, we were able to extract the lifetime change as the temperature was increased (Figure 4.5b). An increase in the the lifetime of $CsPbBr_3$ films with temperature is attributed to increased interaction of the exciton with surface trap states[105]. Thermally activated trapping and de-trapping in the shallow trap states leading to longer lifetimes has been studied at length[106]. This is behavior is also shown in Chapter 2 (Figure 2.11), where an increase in trap-states results in longer lifetimes due to the same phenomenon. We now have all components necessary to probe the coupling in the nanocrystal array by examining the behavior of the diffusivity with temperature. The diffusivity is defined by:

$$D = \frac{L^2}{2\tau} \tag{4.2}$$

Where L is the diffusion length and τ is the average fluorescent lifetime of the quantum dots. Diffusivity is a thermally activated process which results in an increase in diffusivity with

temperature in most systems[101]. This behavior is expected to adhere to the Arrhenius equation. The diffusivity trended opposite to Arrhenius-like behavior (Figure 4.6).

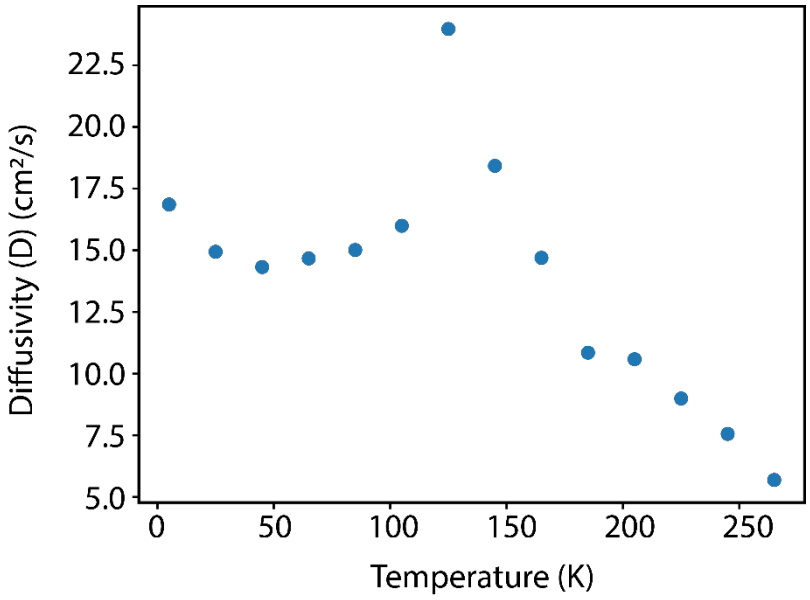

Figure 4.6: The diffusivity of the system vs the temperature in Kelvin

The diffusivity as a function of temperature does not follow the Arrhenius equation. Besides an anamoulous diffusivity at 125 K, likely an outlier, the diffusivity decreases with temperature. This behavior is indicative of high inter-nanocrystal coupling. As temperature increases, the coherence of the collective nanocrystals decreases due to the increase in phonon scattering in the system which leads to a lower diffusivity value. At lower temperatures, exciton delocalization over multiple quantum dots explains the super-like energy transfer, which is suggested by a large diffusivity value. The radiative rate as a function of temperature is critical to the determination of the coherence length. In order to ascertain the radiative rate, it would be necessary to resolve the temperature-dependent PLQY of the nanocrystal array. Using the PLQY and the lifetime, τ, radiative rates can be calculated. By increasing the spacing between the quantum dots and reducing the coupling between them, the same measurements can be performed to verify an increase in the radiative rate in the highly coupled nanocrystal array. The increase in radiative rate at low temperatures is indicative of the merging of the dipole moments of multiple quantum dots.

These experiments prove signatures of high coupling in a 2D array of highly-ordered nanocrystals. To determine the extent of the coupling present, further experiments would need to be completed. Extracting the extent of the delocalization of the exciton is essential to determining if subsequent effects such as superfluorescence and superradiance are present in this system.

Chapter 5: Conclusion and Outlook

We have developed a reproducible synthetic route to near-unity, phase-pure $CsPbBr_3$ nanocrystals by determining the optimal conditions during formation of the nanocrystals. Halide vacancies were confirmed to be the predominant source of charge trapping in sub-critical ratio syntheses. The complex phase diagram of the lead bromide perovskite system plays a large role in the availability of the constituent precursors to passivate deleterious surface states. By exploiting the delicate phase boundaries associated with the various phase stabilities, we were able to extract high quality nanocrystals. A better understanding of the phase diagram of the lead bromide perovskite system can help guide the design of new synthetic strategies to produce nanocrystals with enhanced properties. Overall, this work demonstrates the importance of carefully optimizing the synthetic conditions to achieve high-quality nanocrystals. Future work may focus on optimizing the synthetic method of $CsPbCl_3$ and $CsPbI_3$ nanocrystals to deliver the same quality of nanocrystals. Ultimately, the successful synthesis of highly luminescent, phase-pure nanocrystals has the potential to revolutionize a wide range of technological fields.

We have also observed superraddiance-like behavior in a 2D assembly of these optically efficient nanocrystals. The ultra-high coupling of $CsPbBr_3$ nanocrystals is not restricted to 3D super lattices. Large diffusion distances were observed with a decreasing diffusivity with an increase in temperature. This non-Arrhenius like behavior is indicative of a delocalized exciton over multiple quantum dots and increased coherence at lower temperatures. The increased coherence of the nanocrystals leads to impressive optical feats such as superradiance and superfluorescence. This superradiant and superfluorescent behavior has important implications for the design and optimization of optoelectronic devices. Future work may focus on decreasing the interparticle spacing via ligand exchanges. This would drastically increase coupling between the quantum dots and result in even greater coherent properties and larger diffusion lengths.

Bibliography

(1) Jenkins, T. Physics Education A Brief History of. .. Semiconductors. **2005**.

(2) Suresh, S. Semiconductor Nanomaterials, Methods and Applications: A Review. *Nanosci. Nanotechnol.* **2013**, *3* (3), 62–74. https://doi.org/10.5923/J.NN.20130303.06.

(3) Albanese, A.; Tang, P. S.; Chan, W. C. W. The Effect of Nanoparticle Size, Shape, and Surface Chemistry on Biological Systems. *https://doi.org/10.1146/annurev-bioeng-071811-150124* **2012**, *14*, 1–16. https://doi.org/10.1146/ANNUREV-BIOENG-071811-150124.

(4) Vollath, D.; Fischer, F. D.; Holec, D. Surface Energy of Nanoparticles – Influence of Particle Size and Structure. *Beilstein J. Nanotechnol.* **2018**, *9* (1), 2265. https://doi.org/10.3762/BJNANO.9.211.

(5) Rossetti, R.; Nakahara, S.; Brus, L. E. Quantum Size Effects in the Redox Potentials, Resonance Raman Spectra, and Electronic Spectra of CdS Crystallites in Aqueous Solution. *J. Chem. Phys.* **1998**, *79* (2), 1086. https://doi.org/10.1063/1.445834.

(6) Ciraci, S., Buldum, A. & Batra, I. P. Quantum Effects in Electrical and Thermal Transport through Nanowires. *J. Phys. Condens. Matter* **2001**, *13*, R537.

(7) Kang, M. S.; Sahu, A.; Norris, D. J.; Frisbie, C. D. Size-Dependent Electrical Transport in CdSe Nanocrystal Thin Films. *Nano Lett.* **2010**, *10* (9), 3727–3732. https://doi.org/10.1021/NL102356X/SUPPL_FILE/NL102356X_SI_001.PDF.

(8) Costello, J. B.; O'Hara, S. D.; Wu, Q.; Valovcin, D. C.; Pfeiffer, L. N.; West, K. W.; Sherwin, M. S. Reconstruction of Bloch Wavefunctions of Holes in a Semiconductor. *Nat. 2021 5997883* **2021**, *599* (7883), 57–61. https://doi.org/10.1038/s41586-021-03940-2.

(9) Oba, F.; Kumagai, Y. Design and Exploration of Semiconductors from First Principles: A Review of Recent Advances. *Appl. Phys. Express* **2018**, *11* (6), 060101. https://doi.org/10.7567/APEX.11.060101/XML.

(10) Alivisatos, A. P. Semiconductor Clusters, Nanocrystals, and Quantum Dots. *Science (80-.).* **1996**, *271* (5251), 933–937. https://doi.org/10.1126/SCIENCE.271.5251.933.

(11) Nirmal, M.; Brus, L. Luminescence Photophysics in Semiconductor Nanocrystals. *Acc. Chem. Res.* **1999**, *32* (5), 407–414. https://doi.org/10.1021/AR9700320/ASSET/IMAGES/LARGE/AR9700320F00007.JPEG.

(12) Murray, C. B.; Kagan, C. R.; Bawendi, M. G. Synthesis and Characterization of Monodisperse Nanocrystals and Close-Packed Nanocrystal Assemblies. *https://doi.org/10.1146/annurev.matsci.30.1.545* **2003**, *30*, 545–610. https://doi.org/10.1146/ANNUREV.MATSCI.30.1.545.

(13) Rogach, A. L.; Talapin, D. V; Shevchenko, E. V; Kornowski, A.; Haase, M.; Weller, H.

Organization of Matter on Different Size Scales: Monodisperse Nanocrystals and Their Superstructures**. https://doi.org/10.1002/1616-3028.

(14) Lamer, V. K.; Dinegar, R. H. Theory, Production and Mechanism of Formation of Monodispersed Hydrosols. *J. Am. Chem. Soc.* **1950**, *72* (11), 4847–4854. https://doi.org/10.1021/JA01167A001/ASSET/JA01167A001.FP.PNG_V03.

(15) Murray, C. B.; Norris, D. J.; Bawendi, M. G. Synthesis and Characterization of Nearly Monodisperse CdE (E = S, Se, Te) Semiconductor Nanocrystallites. *J. Am. Chem. Soc* **1993**, *115*, 8706–8715.

(16) Stuczynski, S. M.; Brennan, J. G.; Steigerwald, M. L. Formation of Metal-Chalcogen Bonds by the Reaction of Metal Alkyls with Silyl Chalcogenides. *Inorg. Chem.* **1989**, *28* (25), 4431–4432. https://doi.org/10.1021/IC00324A001/ASSET/IC00324A001.FP.PNG_V03.

(17) Imran, M.; Ijaz, P.; Baranov, D.; Goldoni, L.; Petralanda, U.; Akkerman, Q.; Abdelhady, A. L.; Prato, M.; Bianchini, P.; Infante, I.; Manna, L. Shape-Pure, Nearly Monodispersed CsPbBr 3 Nanocubes Prepared Using Secondary Aliphatic Amines. *Nano Lett.* **2018**, *18* (12), 7822–7831. https://doi.org/10.1021/acs.nanolett.8b03598.

(18) Peng, X.; Wickham, J.; Alivisatos, A. P. Kinetics of II-VI and III-V Colloidal Semiconductor Nanocrystal Growth: "Focusing" of Size Distributions [15]. *J. Am. Chem. Soc.* **1998**, *120* (21), 5343–5344. https://doi.org/10.1021/JA9805425/SUPPL_FILE/JA5343.PDF.

(19) Hendricks, M. P.; Campos, M. P.; Cleveland, G. T.; Plante, I. J. La; Owen, J. S. A Tunable Library of Substituted Thiourea Precursors to Metal Sulfide Nanocrystals. *Science (80-.).* **2015**, *348* (6240), 1226–1230. https://doi.org/10.1126/SCIENCE.AAA2951/SUPPL_FILE/HENDRICKS.SM.PDF.

(20) Sautter, K. E.; Vallejo, K. D.; Simmonds, P. J. Strain-Driven Quantum Dot Self-Assembly by Molecular Beam Epitaxy. *J. Appl. Phys.* **2020**, *128* (3), 031101. https://doi.org/10.1063/5.0012066.

(21) Zhang, D.; Gökce, B.; Barcikowski, S. Laser Synthesis and Processing of Colloids: Fundamentals and Applications. *Chem. Rev.* **2017**, *117* (5), 3990–4103. https://doi.org/10.1021/ACS.CHEMREV.6B00468/ASSET/IMAGES/LARGE/CR-2016-00468N_0042.JPEG.

(22) Bawendi, M. G.; Carroll, P. J.; Wilson, W. L.; Brus, L. E. Luminescence Properties of CdSe Quantum Crystallites: Resonance between Interior and Surface Localized States. *J. Chem. Phys.* **1998**, *96* (2), 946. https://doi.org/10.1063/1.462114.

(23) Roussignol, P.; Ricard, D.; Flytzanis, C.; Neuroth, N. Phonon Broadening and Spectral Hole Burning in Very Small Semiconductor Particles. *Phys. Rev. Lett.* **1989**, *62* (3), 312. https://doi.org/10.1103/PhysRevLett.62.312.

(24) Peyghambarian, N.; Hulin, D.; Joffre, M.; Hulin, D.; Joffre, M.; Migus, A.; Antonetti, A.; Koch, S. W. Femtosecond Optical Nonlinearities of CdSe Quantum Dots. *IEEE J. Quantum Electron.* **1989**, *25* (12), 2516–2522. https://doi.org/10.1109/3.40636.

(25) Egorov, S. A.; Rabani, E.; Berne, B. J. Nonradiative Relaxation Processes in Condensed Phases: Quantum versus Classical Baths. *J. Chem. Phys.* **1999**, *110* (11), 5238. https://doi.org/10.1063/1.478420.

(26) McMurdie, H. F. Chemical and Physical Aspects: The Chemistry of Imperfect Crystals. F. A. Kroger. North-Holland, Amsterdam; Interscience (Wiley), New York, 1964. Xvi + 1039 Pp. $33. *Science (80-.).* **1964**, *145* (3627), 40–41. https://doi.org/10.1126/SCIENCE.145.3627.40.

(27) Maruska, H. P.; Tietjen, J. J. THE PREPARATION AND PROPERTIES OF VAPOR-DEPOSITED SINGLE-CRYSTAL-LINE GaN. *Appl. Phys. Lett.* **2003**, *15* (10), 327. https://doi.org/10.1063/1.1652845.

(28) Pengelly, R. S.; Wood, S. M.; Milligan, J. W.; Sheppard, S. T.; Pribble, W. L. A Review of GaN on SiC High Electron-Mobility Power Transistors and MMICs. *IEEE Trans. Microw. Theory Tech.* **2012**, *60* (6 PART 2), 1764–1783. https://doi.org/10.1109/TMTT.2012.2187535.

(29) Kucharski, R.; Sochacki, T.; Lucznik, B.; Bockowski, M. Growth of Bulk GaN Crystals. *J. Appl. Phys.* **2020**, *128* (5), 050902. https://doi.org/10.1063/5.0009900.

(30) Ip, A. H.; Thon, S. M.; Hoogland, S.; Voznyy, O.; Zhitomirsky, D.; Debnath, R.; Levina, L.; Rollny, L. R.; Carey, G. H.; Fischer, A.; Kemp, K. W.; Kramer, I. J.; Ning, Z.; Labelle, A. J.; Chou, K. W.; Amassian, A.; Sargent, E. H. Hybrid Passivated Colloidal Quantum Dot Solids. *Nat. Nanotechnol. 2012 79* **2012**, *7* (9), 577–582. https://doi.org/10.1038/nnano.2012.127.

(31) Kilina, S. V.; Tamukong, P. K.; Kilin, D. S. Surface Chemistry of Semiconducting Quantum Dots: Theoretical Perspectives. *Acc. Chem. Res.* **2016**, *49* (10), 2127–2135. https://doi.org/10.1021/ACS.ACCOUNTS.6B00196/ASSET/IMAGES/LARGE/AR-2016-00196Z_0005.JPEG.

(32) Gao, Y.; Peng, X. Photogenerated Excitons in Plain Core CdSe Nanocrystals with Unity Radiative Decay in Single Channel: The Effects of Surface and Ligands. *J. Am. Chem. Soc.* **2015**, *137* (12), 4230–4235. https://doi.org/10.1021/JACS.5B01314/ASSET/IMAGES/LARGE/JA-2015-013142_0002.JPEG.

(33) De Nolf, K.; Cosseddu, S. M.; Jasieniak, J. J.; Drijvers, E.; Martins, J. C.; Infante, I.; Hens, Z. Binding and Packing in Two-Component Colloidal Quantum Dot Ligand Shells: Linear versus Branched Carboxylates. *J. Am. Chem. Soc.* **2017**, *139* (9), 3456–3464. https://doi.org/10.1021/JACS.6B11328/ASSET/IMAGES/LARGE/JA-2016-11328D_0006.JPEG.

(34) Stranick, S. J.; Parikh, + A N; Allara, D. L.; Weiss, P. S. A New Mechanism for Surface Diffusion: Motion of a Substrate-Adsorbate Complex. *J. Phys. Chem* **1994**, *98*, 11136–11142.

(35) Kirkwood, N.; Monchen, J. O. V.; Crisp, R. W.; Grimaldi, G.; Bergstein, H. A. C.; Du Fossé, I.; Van Der Stam, W.; Infante, I.; Houtepen, A. J. Finding and Fixing Traps in II-VI and III-V Colloidal Quantum Dots: The Importance of Z-Type Ligand Passivation. *J. Am.*

Chem. Soc. **2018**, *140* (46), 15712–15723. https://doi.org/10.1021/jacs.8b07783.

(36) Chen, O.; Zhao, J.; Chauhan, V. P.; Cui, J.; Wong, C.; Harris, D. K.; Wei, H.; Han, H.-S.; Fukumura, D.; Jain, R. K.; Bawendi, M. G. Compact High-Quality CdSe–CdS Core–Shell Nanocrystals with Narrow Emission Linewidths and Suppressed Blinking. *Nat. Mater.* **2013**, *12* (5), 445–451. https://doi.org/10.1038/nmat3539.

(37) Kamat, P. V. Quantum Dot Solar Cells. Semiconductor Nanocrystals as Light Harvesters†. *J. Phys. Chem. C* **2008**, *112* (48), 18737–18753. https://doi.org/10.1021/JP806791S.

(38) Tachibana, Y.; Akiyama, H. Y.; Ohtsuka, Y.; Torimoto, T.; Kuwabata, S. CdS Quantum Dots Sensitized TiO2 Sandwich Type Photoelectrochemical Solar Cells. *https://doi.org/10.1246/cl.2007.88* **2006**, *36* (1), 88–89. https://doi.org/10.1246/CL.2007.88.

(39) Curutchet, C.; Franceschetti, A.; Zunger, A.; Scholes, G. D. Examining Förster Energy for Semiconductor Nanocrystalline Quantum Dot Donors and Acceptors. *J. Phys. Chem. C* **2008**, *112* (35), 13336–13341. https://doi.org/10.1021/JP805682M/SUPPL_FILE/JP805682M_SI_001.PDF.

(40) Lee, E. M. Y.; Tisdale, W. A.; Willard, A. P. Perspective: Nonequilibrium Dynamics of Localized and Delocalized Excitons in Colloidal Quantum Dot Solids. *J. Vac. Sci. Technol. A* **2018**, *36* (6), 068501. https://doi.org/10.1116/1.5046694/246069.

(41) Spano, F. C.; Mukamel, S. Superradiance in Molecular Aggregates. *J. Chem. Phys.* **1989**, *91* (2), 683–700. https://doi.org/10.1063/1.457174.

(42) Spano, F. C.; Kuklinski, J. R.; Mukamel, S. Temperature-Dependent Superradiant Decay of Excitons in Small Aggregates. *Phys. Rev. Lett.* **1990**, *65* (2), 211. https://doi.org/10.1103/PhysRevLett.65.211.

(43) Wu, X.; Kolar, A.; Chung, J.; Menon, S. G.; Singh, K.; Borregaard, J.; Bernien, H. Nanophotonic Quantum Network Node with Neutral Atoms and an Integrated Telecom Interface. *New J. Phys.* **2020**, *22* (7), 073033. https://doi.org/10.1088/1367-2630/AB98D4.

(44) Alivisatos, A. P.; Johnsson, K. P.; Peng, X.; Wilson, T. E.; Loweth, C. J.; Bruchez, M. P.; Schultz, P. G. Organization of "nanocrystal Molecules" Using DNA. *Nat. 1996 3826592* **1996**, *382* (6592), 609–611. https://doi.org/10.1038/382609a0.

(45) Cui, J.; Panfil, Y. E.; Koley, S.; Shamalia, D.; Waiskopf, N.; Remennik, S.; Popov, I.; Oded, M.; Banin, U. Colloidal Quantum Dot Molecules Manifesting Quantum Coupling at Room Temperature. *Nat. Commun. 2019 101* **2019**, *10* (1), 1–10. https://doi.org/10.1038/s41467-019-13349-1.

(46) Deutsch, Z.; Neeman, L.; Oron, D. Luminescence Upconversion in Colloidal Double Quantum Dots. *Nat. Nanotechnol. 2013 89* **2013**, *8* (9), 649–653. https://doi.org/10.1038/nnano.2013.146.

(47) Lv, B.; Zhang, H.; Wang, L.; Zhang, C.; Wang, X.; Zhang, J.; Xiao, M. Photon Antibunching in a Cluster of Giant CdSe/CdS Nanocrystals. *Nat. Commun. 2018 91* **2018**, *9* (1), 1–7. https://doi.org/10.1038/s41467-018-03971-w.

(48) Imran, M.; Caligiuri, V.; Wang, M.; Goldoni, L.; Prato, M.; Krahne, R.; De Trizio, L.; Manna, L. Benzoyl Halides as Alternative Precursors for the Colloidal Synthesis of Lead-Based Halide Perovskite Nanocrystals. *J. Am. Chem. Soc.* **2018**, *140* (7), 2656–2664. https://doi.org/10.1021/jacs.7b13477.

(49) Bronstein, N. D.; Yao, Y.; Xu, L.; O'Brien, E.; Powers, A. S.; Ferry, V. E.; Alivisatos, A. P.; Nuzzo, R. G. Quantum Dot Luminescent Concentrator Cavity Exhibiting 30-Fold Concentration. *ACS Photonics* **2015**, *2* (11), 1576–1583. https://doi.org/10.1021/ACSPHOTONICS.5B00334/ASSET/IMAGES/PH-2015-00334Q_M004.GIF.

(50) Hanifi, D. A.; Bronstein, N. D.; Koscher, B. A.; Nett, Z.; Swabeck, J. K.; Takano, K.; Schwartzberg, A. M.; Maserati, L.; Vandewal, K.; van de Burgt, Y.; Salleo, A.; Alivisatos, A. P. Redefining Near-Unity Luminescence in Quantum Dots with Photothermal Threshold Quantum Yield. *Science (80-.).* **2019**, *363* (6432), 1199–1202. https://doi.org/10.1126/science.aat3803.

(51) Würth, C.; Grabolle, M.; Pauli, J.; Spieles, M.; Resch-Genger, U. Relative and Absolute Determination of Fluorescence Quantum Yields of Transparent Samples. *Nat. Protoc. 2013 88* **2013**, *8* (8), 1535–1550. https://doi.org/10.1038/nprot.2013.087.

(52) Mannino, G.; Deretzis, I.; Smecca, E.; La Magna, A.; Alberti, A.; Ceratti, D.; Cahen, D. Temperature-Dependent Optical Band Gap in CsPbBr3, MAPbBr3, and FAPbBr3 Single Crystals. *J. Phys. Chem. Lett.* **2020**, *11* (7), 2490–2496. https://doi.org/10.1021/ACS.JPCLETT.0C00295/ASSET/IMAGES/LARGE/JZ0C00295_0004.JPEG.

(53) Kang, J.; Wang, L.-W. High Defect Tolerance in Lead Halide Perovskite CsPbBr 3. **2017**. https://doi.org/10.1021/acs.jpclett.6b02800.

(54) Nenon, D. P.; Pressler, K.; Kang, J.; Koscher, B. A.; Olshansky, J. H.; Osowiecki, W. T.; Koc, M. A.; Wang, L.-W.; Alivisatos, A. P. Design Principles for Trap-Free CsPbX 3 Nanocrystals: Enumerating and Eliminating Surface Halide Vacancies with Softer Lewis Bases. *J. Am. Chem. Soc* **2018**, *140*, 34. https://doi.org/10.1021/jacs.8b11035.

(55) Koscher, B. A.; Swabeck, J. K.; Bronstein, N. D.; Alivisatos, A. P. Essentially Trap-Free $CsPbBr_3$ Colloidal Nanocrystals by Postsynthetic Thiocyanate Surface Treatment. *J. Am. Chem. Soc.* **2017**, *139* (19), 6566–6569. https://doi.org/10.1021/jacs.7b02817.

(56) Zhang, S.; Zhukovskyi, M.; Jankó, B.; Kuno, M. Progress in Laser Cooling Semiconductor Nanocrystals and Nanostructures. *NPG Asia Mater. 2019 111* **2019**, *11* (1), 1–19. https://doi.org/10.1038/s41427-019-0156-4.

(57) Protesescu, L.; Yakunin, S.; Bodnarchuk, M. I.; Krieg, F.; Caputo, R.; Hendon, C. H.; Yang, R. X.; Walsh, A.; Kovalenko, M. V. Nanocrystals of Cesium Lead Halide Perovskites (CsPbX 3 , X = Cl, Br, and I): Novel Optoelectronic Materials Showing Bright Emission with Wide Color Gamut. *Nano Lett* **2015**, *15*. https://doi.org/10.1021/nl5048779.

(58) Dutta, A.; Behera, R. K.; Pal, P.; Baitalik, S.; Pradhan, N. Near-Unity Photoluminescence Quantum Efficiency for All CsPbX 3 (X=Cl, Br, and I) Perovskite Nanocrystals: A

Generic Synthesis Approach . *Angew. Chemie* **2019**, *131* (17), 5608–5612. https://doi.org/10.1002/ange.201900374.

(59) Woo, J. Y.; Kim, Y.; Bae, J.; Kim, T. G.; Kim, J. W.; Lee, D. C.; Jeong, S. Highly Stable Cesium Lead Halide Perovskite Nanocrystals through in Situ Lead Halide Inorganic Passivation. *Chem. Mater.* **2017**, *29* (17), 7088–7092. https://doi.org/10.1021/ACS.CHEMMATER.7B02669/SUPPL_FILE/CM7B02669_SI_001.PDF.

(60) Li, F.; Liu, Y.; Wang, H.; Zhan, Q.; Liu, Q.; Xia, Z. Postsynthetic Surface Trap Removal of CsPbX3 (X = Cl, Br, or I) Quantum Dots via a ZnX2/Hexane Solution toward an Enhanced Luminescence Quantum Yield. *Chem. Mater.* **2018**, *30* (23), 8546–8554. https://doi.org/10.1021/ACS.CHEMMATER.8B03442/SUPPL_FILE/CM8B03442_SI_001.PDF.

(61) Rainoì, G.; Nedelcu, G.; Protesescu, L.; Bodnarchuk, M. I.; Kovalenko, M. V.; Mahrt, R. F.; Stöferle, T. Single Cesium Lead Halide Perovskite Nanocrystals at Low Temperature: Fast Single-Photon Emission, Reduced Blinking, and Exciton Fine Structure. *ACS Nano* **2016**, *10* (2), 2485–2490. https://doi.org/10.1021/ACSNANO.5B07328/ASSET/IMAGES/LARGE/NN-2015-073283_0006.JPEG.

(62) Bae, W. K.; Padilha, L. A.; Park, Y. S.; McDaniel, H.; Robel, I.; Pietryga, J. M.; Klimov, V. I. Controlled Alloying of the Core-Shell Interface in CdSe/CdS Quantum Dots for Suppression of Auger Recombination. *ACS Nano* **2013**, *7* (4), 3411–3419. https://doi.org/10.1021/NN4002825/SUPPL_FILE/NN4002825_SI_001.PDF.

(63) Kagan, C. R.; Murray, C. B.; Nirmal, M.; Bawendi, M. G. Electronic Energy Transfer in CdSe Quantum Dot Solids. **1996**.

(64) Kagan, C. R.; Murray, C. B.; Bawendi, M. G. Long-Range Resonance Transfer of Electronic Excitations in Close-Packed CdSe Quantum-Dot Solids. **1996**.

(65) Xu, F.; Ma, X.; Haughn, C. R.; Benavides, J.; Doty, M. F.; Cloutier, S. G. Efficient Exciton Funneling in Cascaded PbS Quantum Dot Superstructures. **2011**. https://doi.org/10.1021/nn203728t.

(66) Dahl, J. C.; Wang, X.; Huang, X.; Chan, E. M.; Alivisatos, A. P. Elucidating the Weakly Reversible Cs-Pb-Br Perovskite Nanocrystal Reaction Network with High-Throughput Maps and Transformations. *J. Am. Chem. Soc.* **2020**, *142* (27), 11915–11926. https://doi.org/10.1021/JACS.0C04997/SUPPL_FILE/JA0C04997_SI_001.PDF.

(67) Bekenstein, Y.; Koscher, B. A.; Eaton, S. W.; Yang, P.; Alivisatos, A. P. Highly Luminescent Colloidal Nanoplates of Perovskite Cesium Lead Halide and Their Oriented Assemblies. *J. Am. Chem. Soc.* **2015**, *137* (51), 16008–16011. https://doi.org/10.1021/jacs.5b11199.

(68) Akkerman, Q. A.; Motti, S. G.; Srimath Kandada, A. R.; Mosconi, E.; D'Innocenzo, V.; Bertoni, G.; Marras, S.; Kamino, B. A.; Miranda, L.; De Angelis, F.; Petrozza, A.; Prato, M.; Manna, L. Solution Synthesis Approach to Colloidal Cesium Lead Halide Perovskite Nanoplatelets with Monolayer-Level Thickness Control. *J. Am. Chem. Soc.* **2016**, *138* (3),

1010–1016. https://doi.org/10.1021/JACS.5B12124/ASSET/IMAGES/LARGE/JA-2015-12124D_0004.JPEG.

(69) Zhang, D.; Eaton, S. W.; Yu, Y.; Dou, L.; Yang, P. Solution-Phase Synthesis of Cesium Lead Halide Perovskite Nanowires. *J. Am. Chem. Soc.* **2015**, *137* (29), 9230–9233. https://doi.org/10.1021/jacs.5b05404.

(70) Imran, M.; Di Stasio, F.; Dang, Z.; Canale, C.; Khan, A. H.; Shamsi, J.; Brescia, R.; Prato, M.; Manna, L. Colloidal Synthesis of Strongly Fluorescent CsPbBr3Nanowires with Width Tunable down to the Quantum Confinement Regime. *Chem. Mater.* **2016**, *28* (18), 6450–6454. https://doi.org/10.1021/ACS.CHEMMATER.6B03081/ASSET/IMAGES/LARGE/CM-2016-030814_0005.JPEG.

(71) Song, J.; Xu, L.; Li, J.; Xue, J.; Dong, Y.; Li, X.; Zeng, H. Monolayer and Few-Layer All-Inorganic Perovskites as a New Family of Two-Dimensional Semiconductors for Printable Optoelectronic Devices. *Adv. Mater.* **2016**, *28* (24), 4861–4869. https://doi.org/10.1002/ADMA.201600225.

(72) Shamsi, J.; Dang, Z.; Bianchini, P.; Canale, C.; Stasio, F. Di; Brescia, R.; Prato, M.; Manna, L. Colloidal Synthesis of Quantum Confined Single Crystal CsPbBr3 Nanosheets with Lateral Size Control up to the Micrometer Range. *J. Am. Chem. Soc.* **2016**, *138* (23), 7240–7243. https://doi.org/10.1021/JACS.6B03166/ASSET/IMAGES/LARGE/JA-2016-03166K_0003.JPEG.

(73) Sun, S.; Yuan, D.; Xu, Y.; Wang, A.; Deng, Z. Ligand-Mediated Synthesis of Shape-Controlled Cesium Lead Halide Perovskite Nanocrystals via Reprecipitation Process at Room Temperature. *ACS Nano* **2016**, *10* (3), 3648–3657. https://doi.org/10.1021/ACSNANO.5B08193/ASSET/IMAGES/NN-2015-081936_M002.GIF.

(74) Zhang, D.; Yu, Y.; Bekenstein, Y.; Wong, A. B.; Alivisatos, A. P.; Yang, P. Ultrathin Colloidal Cesium Lead Halide Perovskite Nanowires. *J. Am. Chem. Soc.* **2016**, *138* (40), 13155–13158. https://doi.org/10.1021/JACS.6B08373/ASSET/IMAGES/LARGE/JA-2016-08373Y_0004.JPEG.

(75) Bohn, B. J.; Tong, Y.; Gramlich, M.; Lai, M. L.; Döblinger, M.; Wang, K.; Hoye, R. L. Z.; Müller-Buschbaum, P.; Stranks, S. D.; Urban, A. S.; Polavarapu, L.; Feldmann, J. Boosting Tunable Blue Luminescence of Halide Perovskite Nanoplatelets through Postsynthetic Surface Trap Repair. *Nano Lett.* **2018**, *18* (8), 5231–5238. https://doi.org/10.1021/ACS.NANOLETT.8B02190/ASSET/IMAGES/LARGE/NL-2018-02190Z_0004.JPEG.

(76) Pan, A.; He, B.; Fan, X.; Liu, Z.; Urban, J. J.; Alivisatos, A. P.; He, L.; Liu, Y. Insight into the Ligand-Mediated Synthesis of Colloidal CsPbBr3 Perovskite Nanocrystals: The Role of Organic Acid, Base, and Cesium Precursors. *ACS Nano* **2016**, *10* (8), 7943–7954. https://doi.org/10.1021/ACSNANO.6B03863/ASSET/IMAGES/LARGE/NN-2016-03863G_0009.JPEG.

(77) Almeida, G.; Goldoni, L.; Akkerman, Q.; Dang, Z.; Khan, A. H.; Marras, S.; Moreels, I.;

Manna, L. Role of Acid-Base Equilibria in the Size, Shape, and Phase Control of Cesium Lead Bromide Nanocrystals. *ACS Nano* **2018**, *12* (2), 1704–1711. https://doi.org/10.1021/ACSNANO.7B08357/ASSET/IMAGES/NN-2017-08357N_M004.GIF.

(78) Liu, Z.; Bekenstein, Y.; Ye, X.; Nguyen, S. C.; Swabeck, J.; Zhang, D.; Lee, S. T.; Yang, P.; Ma, W.; Alivisatos, A. P. Ligand Mediated Transformation of Cesium Lead Bromide Perovskite Nanocrystals to Lead Depleted Cs4PbBr6 Nanocrystals. *J. Am. Chem. Soc.* **2017**, *139* (15), 5309–5312. https://doi.org/10.1021/JACS.7B01409/ASSET/IMAGES/LARGE/JA-2017-01409D_0004.JPEG.

(79) Udayabhaskararao, T.; Houben, L.; Cohen, H.; Menahem, M.; Pinkas, I.; Avram, L.; Wolf, T.; Teitelboim, A.; Leskes, M.; Yaffe, O.; Oron, D.; Kazes, M. A Mechanistic Study of Phase Transformation in Perovskite Nanocrystals Driven by Ligand Passivation. *Chem. Mater.* **2018**, *30* (1), 84–93. https://doi.org/10.1021/ACS.CHEMMATER.7B02425/ASSET/IMAGES/LARGE/CM-2017-02425U_0009.JPEG.

(80) Kongkanand, A.; Tvrdy, K.; Takechi, K.; Kuno, M.; Kamat, P. V. Quantum Dot Solar Cells. Tuning Photoresponse through Size and Shape Control of CdSe-TiO2 Architecture. *J. Am. Chem. Soc.* **2008**, *130* (12), 4007–4015. https://doi.org/10.1021/JA0782706/SUPPL_FILE/JA0782706-FILE005.PDF.

(81) Kang, J.; Wang, L. W. High Defect Tolerance in Lead Halide Perovskite CsPbBr3. *J. Phys. Chem. Lett.* **2017**, *8* (2), 489–493. https://doi.org/10.1021/acs.jpclett.6b02800.

(82) Mehetor, S. K.; Ghosh, H.; Pradhan, N. Acid-Amine Equilibria for Formation and Long-Range Self-Organization of Ultrathin CsPbBr 3 Perovskite Platelets. *J. Phys. Chem. Lett.* **2019**, *10* (6), 1300–1305. https://doi.org/10.1021/ACS.JPCLETT.9B00333/ASSET/IMAGES/LARGE/JZ-2019-00333E_0005.JPEG.

(83) Weidman, M. C.; Seitz, M.; Stranks, S. D.; Tisdale, W. A. Highly Tunable Colloidal Perovskite Nanoplatelets through Variable Cation, Metal, and Halide Composition. *ACS Nano* **2016**, *10* (8), 7830–7839. https://doi.org/10.1021/ACSNANO.6B03496/SUPPL_FILE/NN6B03496_SI_002.MPG.

(84) Weidman, M. C.; Goodman, A. J.; Tisdale, W. A. Colloidal Halide Perovskite Nanoplatelets: An Exciting New Class of Semiconductor Nanomaterials. *Chem. Mater.* **2017**, *29* (12), 5019–5030. https://doi.org/10.1021/ACS.CHEMMATER.7B01384/ASSET/IMAGES/LARGE/CM-2017-01384V_0008.JPEG.

(85) Dahl, Jakob C; Wang, Xingzhi; Chan, Emory M.; Alivisatos, A. P. High-Throughput Synthesis and Transformations of CsPbBr Nanocrystals Characterized by UV-Vis Absorption and Fluorescence. *Dryad*. https://doi.org/https://doi.org/10.6078/D1XT4F.

(86) Lan, J.; Luo, L.; Wang, M.; Li, F.; Wu, X.; Wang, F. One Pot Gram-Scale Synthesis of CsPbBr3 Nanocrystals and Their Application in Green LED. *J. Lumin.* **2019**, *210*, 464–

471. https://doi.org/10.1016/J.JLUMIN.2019.03.014.

(87) Ng, C. K.; Yin, W.; Li, H.; Jasieniak, J. J. Scalable Synthesis of Colloidal CsPbBr3 Perovskite Nanocrystals with High Reaction Yields through Solvent and Ligand Engineering. *Nanoscale* **2020**, *12* (8), 4859–4867. https://doi.org/10.1039/C9NR10726F.

(88) Zhu, J.; Zhu, Y.; Huang, J.; Gong, Y.; Shen, J.; Li, C. Synthesis of CsPbBr3 Perovskite Nanocrystals with the Sole Ligand of Protonated (3-Aminopropyl)Triethoxysilane. *J. Mater. Chem. C* **2019**, *7* (24), 7201–7206. https://doi.org/10.1039/C9TC02089F.

(89) Xu, Y.; Zhang, Q.; Lv, L.; Han, W.; Wu, G.; Yang, D.; Dong, A. Synthesis of Ultrasmall CsPbBr3 Nanoclusters and Their Transformation to Highly Deep-Blue-Emitting Nanoribbons at Room Temperature. *Nanoscale* **2017**, *9* (44), 17248–17253. https://doi.org/10.1039/C7NR06959F.

(90) Kwon, Y.; Kim, S. Indium Phosphide Magic-Sized Clusters: Chemistry and Applications. *NPG Asia Mater. 2021 131* **2021**, *13* (1), 1–16. https://doi.org/10.1038/s41427-021-00300-4.

(91) Yu, Q.; Liu, C. Y. Study of Magic-Size-Cluster Mediated Formation of Cds Nanocrystals: Properties of the Magic-Size Clusters and Mechanism Implication. *J. Phys. Chem. C* **2009**, *113* (29), 12766–12771. https://doi.org/10.1021/JP903199Y/SUPPL_FILE/JP903199Y_SI_001.PDF.

(92) Penzo, E.; Loiudice, A.; Barnard, E. S.; Borys, N. J.; Jurow, M. J.; Lorenzon, M.; Rajzbaum, I.; Wong, E. K.; Liu, Y.; Schwartzberg, A. M.; Cabrini, S.; Whitelam, S.; Buonsanti, R.; Weber-Bargioni, A. Long-Range Exciton Diffusion in Two-Dimensional Assemblies of Cesium Lead Bromide Perovskite Nanocrystals. *ACS Nano* **2020**, *14* (6), 6999–7007. https://doi.org/10.1021/ACSNANO.0C01536/ASSET/IMAGES/LARGE/NN0C01536_0003.JPEG.

(93) Akselrod, G. M.; Prins, F.; Poulikakos, L. V.; Lee, E. M. Y.; Weidman, M. C.; Mork, A. J.; Willard, A. P.; Bulović, V.; Tisdale, W. A. Subdiffusive Exciton Transport in Quantum Dot Solids. *Nano Lett.* **2014**, *14* (6), 3556–3562. https://doi.org/10.1021/NL501190S/SUPPL_FILE/NL501190S_SI_001.PDF.

(94) Kholmicheva, N.; Moroz, P.; Bastola, E.; Razgoniaeva, N.; Bocanegra, J.; Shaughnessy, M.; Porach, Z.; Khon, D.; Zamkov, M. Mapping the Exciton Diffusion in Semiconductor Nanocrystal Solids. *ACS Nano* **2015**, *9* (3), 2926–2937. https://doi.org/10.1021/NN507322Y/SUPPL_FILE/NN507322Y_SI_001.PDF.

(95) Kholmicheva, N.; Moroz, P.; Eckard, H.; Jensen, G.; Zamkov, M. Energy Transfer in Quantum Dot Solids. *ACS Energy Lett.* **2017**, *2* (1), 154–160. https://doi.org/10.1021/ACSENERGYLETT.6B00569/ASSET/IMAGES/LARGE/NZ-2016-00569C_0005.JPEG.

(96) Rainò, G.; Becker, M. A.; Bodnarchuk, M. I.; Mahrt, R. F.; Kovalenko, M. V.; Stöferle, T. Superfluorescence from Lead Halide Perovskite Quantum Dot Superlattices. *Nat. 2018 5637733* **2018**, *563* (7733), 671–675. https://doi.org/10.1038/s41586-018-0683-0.

(97) Cherniukh, I.; Rainò, G.; Stöferle, T.; Burian, M.; Travesset, A.; Naumenko, D.; Amenitsch, H.; Erni, R.; Mahrt, R. F.; Bodnarchuk, M. I.; Kovalenko, M. V. Perovskite-Type Superlattices from Lead Halide Perovskite Nanocubes. *Nat. 2021 5937860* **2021**, *593* (7860), 535–542. https://doi.org/10.1038/s41586-021-03492-5.

(98) Diroll, B. T.; Zhou, H.; Schaller, R. D. Low-Temperature Absorption, Photoluminescence, and Lifetime of CsPbX3 (X = Cl, Br, I) Nanocrystals. *Adv. Funct. Mater.* **2018**, *28* (30), 1800945. https://doi.org/10.1002/ADFM.201800945.

(99) Shcherbakov-Wu, W.; Sercel, P. C.; Krieg, F.; Kovalenko, M. V.; Tisdale, W. A. Temperature-Independent Dielectric Constant in CsPbBr3Nanocrystals Revealed by Linear Absorption Spectroscopy. *J. Phys. Chem. Lett.* **2021**, *12* (33), 8088–8095. https://doi.org/10.1021/ACS.JPCLETT.1C01822/ASSET/IMAGES/LARGE/JZ1C01822_0004.JPEG.

(100) Blach, D. D.; Lumsargis, V. A.; Clark, D. E.; Chuang, C.; Wang, K.; Dou, L.; Schaller, R. D.; Cao, J.; Li, C. W.; Huang, L. Superradiance and Exciton Delocalization in Perovskite Quantum Dot Superlattices. *Nano Lett.* **2022**, *22* (19), 7811–7818. https://doi.org/10.1021/ACS.NANOLETT.2C02427/ASSET/IMAGES/LARGE/NL2C02427_0004.JPEG.

(101) Wuelfing, W. P.; Murray, R. W. Electron Hopping through Films of Arenethiolate Monolayer-Protected Gold Clusters. *J. Phys. Chem. B* **2002**, *106* (12), 3139–3145. https://doi.org/10.1021/JP013987F/SUPPL_FILE/JP013987F_S.PDF.

(102) Man, M. T.; Lee, H. S. Discrete States and Carrier-Phonon Scattering in Quantum Dot Population Dynamics. *Sci. Reports 2015 51* **2015**, *5* (1), 1–6. https://doi.org/10.1038/srep08267.

(103) Fennel, F.; Lochbrunner, S. Förster-Mediated Spectral Diffusion in Disordered Organic Materials. *Phys. Rev. B - Condens. Matter Mater. Phys.* **2012**, *85* (9), 094203. https://doi.org/10.1103/PHYSREVB.85.094203/FIGURES/10/MEDIUM.

(104) Shcherbakov-Wu, W.; Saris, S.; Sheehan, T.; Wong, N. N.; Powers, E. R.; Krieg, F.; Kovalenko, M. V; Willard, A. P.; Tisdale, W. A. Persistent Enhancement of Exciton Diffusivity in CsPbBr 3 Nanocrystal Solids.

(105) Yuan, X.; Jing, P.; Li, J.; Wei, M.; Hua, J.; Zhao, J.; Tian, L.; Li, J. Temperature-Dependent Photoluminescence of Inorganic Perovskite Nanocrystal Films. *RSC Adv.* **2016**, *6* (82), 78311–78316. https://doi.org/10.1039/C6RA17008K.

(106) Rodà, C.; Fasoli, M.; Zaffalon, M. L.; Cova, F.; Pinchetti, V.; Shamsi, J.; Abdelhady, A. L.; Imran, M.; Meinardi, F.; Manna, L.; Vedda, A.; Brovelli, S.; Rodà, C.; Fasoli, M.; Zaffalon, M. L.; Cova, F.; Pinchetti, V.; Meinardi, F.; Vedda, A.; Brovelli, S.; Shamsi, J.; Abdelhady, A. L.; Imran, M.; Manna, L. Understanding Thermal and A-Thermal Trapping Processes in Lead Halide Perovskites Towards Effective Radiation Detection Schemes. *Adv. Funct. Mater.* **2021**, *31* (43), 2104879. https://doi.org/10.1002/ADFM.202104879.